Do intrinsic functional networks reflect interacting brain rhythms? Assessing the power bias in MEG amplitude connectivity at rest

Alix Cordier[a], Alison Mary[b], Marc Vander Ghinst[a,c], Serge Goldman[a,d], Xavier De Tiège[a,e], Vincent Wens[a,e]

[a] Université libre de Bruxelles (ULB), ULB Neuroscience Institute (UNI), Laboratoire de Neuroanatomie et Neuroimagerie translationnelles (LN^{2}T), Brussels, Belgium.

[b] Université libre de Bruxelles (ULB), ULB Neuroscience Institute (UNI), Neuropsychology and Functional Neuroimaging Research Unit (UR2NF) at Centre de Recherches Cognition et Neurosciences (CRCN), Brussels, Belgium.

[c] Université libre de Bruxelles (ULB), Hôpital Universitaire de Bruxelles (HUB), CUB Hôpital Erasme, Department of Ear, Nose and Throat, and of Cervico-facial surgery, Brussels, Belgium.

[d] Université libre de Bruxelles (ULB), Hôpital Universitaire de Bruxelles (HUB), CUB Hôpital Erasme, Department of Nuclear Medicine, Brussels, Belgium.

[e] Université libre de Bruxelles (ULB), Hôpital Universitaire de Bruxelles (HUB), CUB Hôpital Erasme, Department of Translational Neuroimaging, Brussels, Belgium.

Corresponding author: Alix Cordier, Laboratoire de Neuroanatomie et Neuroimagerie translationnelles (LN^{2}T), Route de Lennik 808, 1070 Brussels, Belgium.

E-mail: alix.cordier@ulb.be

Abstract

Electrophysiological measures of functional connectivity can be affected by the power bias, i.e., variations in their estimation due to variations in the signal-to-noise ratio (SNR) rather than in genuine neural interactions. Intrinsic functional networks emerge at rest from magnetoencephalography (MEG) amplitude connectivity mostly within the α and β frequency bands, where the SNR of MEG recordings is coincidentally maximal. This raises the question, is the spectral specificity of these networks really driven by neural oscillatory dynamics or is it an artifact due to the power bias? Here, we present a detailed theoretical analysis of the power bias in amplitude connectivity allowing to disentangle the neural part of connectivity from the nonlinear SNR dependence of estimated amplitude connectivity (as well as from the contribution of noise correlations). On this basis, we developed a new correction technique involving a SNR-dependent renormalization of amplitude connectivity, which we validated using synthetic data. We then applied the technique to resting-state MEG data and quantified to what extent the power bias affects the spectral content of intrinsic functional brain couplings. We demonstrated the absence of such effect, which was explained by the observation in synthetic data that the power bias is very reduced at the sufficiently high SNRs found in resting-state MEG recordings. Comparison with a classical linear regression technique highlights the importance of our nonlinear correction to reach this conclusion. Our analysis thus confirms the crucial role of neural oscillations for the spontaneous emergence of intrinsic brain functional networks.

Keywords: power bias, magnetoencephalography, resting-state functional connectivity, intrinsic functional network, brain rhythm

1. Introduction

The notion that human brain function is organized into intrinsic functional networks (Engel et al., 2013) emerging from and sustained by spontaneously interacting assemblies of neurons, has arguably become a central theme of human neuroscience (Deco and Corbetta, 2011; Fox and Raichle, 2007). Research on these brain networks has evolved tremendously since their first discovery using resting-state functional magnetic resonance imaging (fMRI) (Biswal et al., 1995; Fox et al., 2005) and the identification of coupled brain rhythms as their electrophysiological signature using resting-state magnetoencephalography (MEG) (Brookes et al., 2011; de Pasquale et al., 2010; Hipp et al., 2012). A wealth of knowledge has accumulated on diverse aspects of their electrophysiology, such as the spectral specificity of resting-state networks (Brookes et al., 2014, 2016; Tewarie et al., 2016; Wens et al., 2014a), the existence of supra-second-scale dynamics underlying versatile global network topology (de Pasquale et al., 2012, 2016; Della Penna et al., 2019) and metastable cross-network couplings (Wens et al., 2019), or their relationship to sub-second bursts of transient brain oscillations (Baker et al., 2014; Coquelet et al., 2022; Seedat et al., 2020; Vidaurre et al., 2018). Several studies also revealed their role in stimulus processing (Betti et al., 2018; Hawellek et al., 2013; Smith et al., 2009), task performance (O'Neill et al., 2015b; O'Neill et al., 2017; Quinn et al., 2018), learning and memory (Higgins et al., 2021; Mary et al., 2017; Roshchupkina et al., 2022; Van Dyck et al., 2021b), and in the pathophysiology of brain disorders (Brookes et al., 2018; Naeije et al., 2019; Puttaert et al., 2020; Sitnikova et al., 2018; Sjøgård et al., 2020; Van Dyck et al., 2021a; Van Schependom et al., 2019).

A key feature of this body of work is its focus on the oscillatory amplitude of neural assemblies, which tracks the spontaneous rise and fall of transient brain rhythms (Hari and Salmelin, 1997; van Ede et al., 2018), and in particular on amplitude envelope correlation (AEC) as electrophysiological marker of their functional connectivity (O'Neill et al., 2015a; Sadaghiani et al., 2022; Siegel et al., 2012). The AEC quantifies to what extent oscillations in distinct brain areas tend to burst simultaneously (Seedat et al., 2020). As such, it differs from phase-based connectivity indices (e.g., coherence and phase-locking value), which rather probe the precise time lag between these oscillations (Fries, 2005; Siegel et al., 2012). By design, both amplitude and phase connectivity assume that functional networks reflect coupled neural oscillations; yet this fundamental assumption may be questioned. Conventional wisdom holds that signal-to-noise ratio (SNR) artificially modulates connectivity estimation (Muthukumaraswamy and Singh, 2011; O'Neill et al., 2015b), an effect that we shall refer to as the *power bias*. The fact that MEG functional networks are best delineated in the α (8–12 Hz) and the β (12–30 Hz) frequency bands (Brookes et al., 2011; Hipp et al., 2012; Wens et al., 2014a), precisely where resting-state MEG signals exhibit their highest SNR (Hari and Salmelin, 1997), may thus legitimately cast some doubt on the oscillatory nature of MEG connectivity. Indeed, MEG connectivity could appear smaller in the lower (δ, θ) and higher (γ) frequency bands not because it is genuinely smaller but because MEG recordings are noisier in these bands, leading to connectivity underestimation. In other words, the possibility remains that intrinsic functional connectivity is broadband rather than carried by specific brain rhythms. This hypothesis was actually raised on fairly different grounds by Hipp and Siegel (2015) using a comparison of fMRI and MEG functional connectomes. Experimental findings of broadband connectivity would have a strong impact

on our conceptual understanding of the electrophysiological mechanisms of functional connectivity (Cabral et al., 2014a; Deco et al., 2011).

In this paper, we sought to confirm or infirm the broadband connectivity hypothesis by directly disentangling the effect of the power bias from AEC estimation. To that aim, we developed a new model-based technique allowing reconstruction of AEC estimates free from the power bias, through a suitable SNR-dependent renormalization of measured AEC estimates. We first assessed the efficiency of the correction using simulations and then applied it to spectrally-resolved AEC of resting-state MEG recordings. This allowed us to examine quantitatively how the power bias affects the connectivity spectrum of intrinsic functional networks and thereby answer our main question. Since our model of AEC power bias turns out to be nonlinear in the SNR, we also compared results with another correction based on a more conventional linear regression approach.

Given the coincidence of functional connectivity and power spectra, and following Hipp and Siegel (2015), we expected that corrected AEC spectra would be flatter and broader-band than previously reported. On the other hand, we had no hard prediction on the degree of these modifications or whether data would agree or disagree with the assumption that intrinsic functional networks reflect interacting neural oscillations.

2. Theory

In this section, we develop the mathematical model that determines how the power bias affects AEC. As a preliminary, we start with the simplest case of linear correlation, as it allows to illustrate clearly key features of the connectivity power bias and how a renormalization of

functional connectivity enables to correct the bias. Simulations illustrating the theory and examining its validity, as well as applications to resting-state MEG data, are described in sections 3 and 4.

2.1. Warm-up: Linear correlation

The linear correlation R between two signals $x = x(t)$ and $y = y(t)$ is given by

$$R = \mathrm{corr}[x, y] = \frac{\mathrm{cov}(x, y)}{\sigma_x \sigma_y}. \tag{1}$$

This corresponds to the covariance $\mathrm{cov}(x, y) = \langle xy \rangle - \langle x \rangle \langle y \rangle$ of x and y suitably normalized by their standard deviation $\sigma_x = \sqrt{\langle x^2 \rangle - \langle x \rangle^2}$ and $\sigma_y = \sqrt{\langle y^2 \rangle - \langle y \rangle^2}$. Brackets $\langle \cdot \rangle$ denote time averaging. In our context, x and y represent experimental MEG signals reconstructed at two distinct brain locations. They can be decomposed as sums of the true cerebral signal (respectively denoted hereafter as x_0 and y_0) and measurement noise (respectively ϵ_x and ϵ_y), i.e.,

$$x = x_0 + \epsilon_x \,, \;\; y = y_0 + \epsilon_y \,. \tag{2}$$

These simple-looking equations entail the hidden assumption that x_0 and y_0 are not mixed, as would be expected after source projection due to the spatial leakage effect (Wens, 2015). We shall keep it that way since all our connectivity estimations will include spatial leakage correction beforehand (Wens et al., 2015; see also section 3).

Our goal is to express the measured correlation (1) in terms of the neural part

$$R_0 = \mathrm{corr}[x_0, y_0] = \frac{\mathrm{cov}(x_0, y_0)}{\sigma_{x_0}\sigma_{y_0}} \tag{3}$$

of the correlation, the SNR estimates

$$\mathrm{SNR}_x = \frac{\sigma_x}{\sigma_{\epsilon_x}}, \qquad \mathrm{SNR}_y = \frac{\sigma_y}{\sigma_{\epsilon_y}}, \tag{4}$$

and possible correlations $R_{\mathrm{noise}} = \mathrm{corr}\left[\epsilon_x, \epsilon_y\right]$ among source-projected measurement noises.

To discover this relationship, we expand the numerator in the right-hand side of Eq. (1),

$$\mathrm{cov}(x, y) = \mathrm{cov}(x_0, y_0) + \mathrm{cov}\left(x_0, \epsilon_y\right) + \mathrm{cov}(\epsilon_x, y_0) + \mathrm{cov}\left(\epsilon_x, \epsilon_y\right).$$

The two middle terms must vanish since cerebral signals x_0, y_0 and measurement noise ϵ_x, ϵ_y are independent, leaving $\mathrm{cov}(x, y) = \mathrm{cov}(x_0, y_0) + \mathrm{cov}\left(\epsilon_x, \epsilon_y\right)$. Similarly, in the denominator

$$\sigma_x^2 = \sigma_{x_0}^2 + 2\mathrm{cov}(x_0, \epsilon_x) + \sigma_{\epsilon_x}^2 = \sigma_{x_0}^2 + \sigma_{\epsilon_x}^2.$$

Combined with definition (4), this equation can be recast as

$$\frac{1}{\sigma_x^2} = \frac{1}{\sigma_x^2}\left(\frac{\sigma_x^2 - \sigma_{\epsilon_x}^2}{\sigma_{x_0}^2}\right) = \frac{1 - \sigma_{\epsilon_x}^2/\sigma_x^2}{\sigma_{x_0}^2} = \frac{1 - \mathrm{SNR}_x^{-2}}{\sigma_{x_0}^2},$$

the factor between parentheses being equal to one. A similar equation holds for the signal y. Plugging these results back into Eq. (1) leads to the sought relationship

$$R = R_0\sqrt{1 - \mathrm{SNR}_x^{-2}}\sqrt{1 - \mathrm{SNR}_y^{-2}} + \frac{R_{\mathrm{noise}}}{\mathrm{SNR}_x\mathrm{SNR}_y}. \tag{6}$$

The correlation R can thus be decomposed into two distinct terms. The first encapsulates the power bias phenomenon and illustrates general features that we discuss now, momentarily

assuming that noise correlations do not contribute ($R_{\text{noise}} = 0$). First, the power bias leads to an underestimation of functional connectivity magnitude, $|R| < |R_0|$. This effect is worst when noise dominates over cerebral activity ($\text{SNR}_x \approx 1$ or $\text{SNR}_y \approx 1$, so $R \approx 0$) but is negligible when cerebral activity dominates ($\text{SNR}_x \gg 1$ and $\text{SNR}_y \gg 1$, so $R \approx R_0$). Second, this underestimation occurs through a SNR-dependent multiplicative factor. This is precisely what allows to disentangle the power bias from genuine functional connectivity, which can be recovered as a suitably renormalized version of the connectivity measure. In the present case, and restoring the possibility of noise correlations, the *renormalized* correlation

$$R_{\text{ren}} = \frac{R - \frac{R_{\text{noise}}}{\text{SNR}_x \text{SNR}_y}}{\sqrt{1 - \text{SNR}_x^{-2}}\sqrt{1 - \text{SNR}_y^{-2}}} \tag{7}$$

indeed allows to recover the neural correlation, $R_{\text{ren}} = R_0$. Of notice, the renormalization factor (i.e., the denominator in Eq. 7) depends nonlinearly on the SNRs, indicating that conventional multiple regression modeling may not be able to efficiently correct the power bias.

On top of the power bias itself, noise correlations contribute additively to functional connectivity estimates but their contribution is dampened at high SNR (second term in Eq. 6). In our context where the noise signals ϵ_x and ϵ_y represent MEG sensor measurement noise projected at two source locations, spurious linear noise correlations are bound to emerge from linear mixing. We can expect spatial leakage correction to suppress these correlations, and thus the power bias to be the dominating feature; still noise correlations

may persist. Their effect can be eliminated by mere subtraction (see numerator in Eq. 7) alongside the power bias renormalization *per se*.

To make the correction procedure applicable in practice, the SNR-dependent renormalization factor (as well as the noise correlation subtractive term) must be expressible in terms of parameters that are accessible to experimental data. That is why we avoided formulating equations (6) and (7) in terms of, e.g., σ_{x_0} and σ_{y_0} since the cerebral signals are unknown. The noise time courses $\epsilon_x(t)$ and $\epsilon_y(t)$ are also inaccessible, but fortunately their variances $\sigma^2_{\epsilon_x}$ and $\sigma^2_{\epsilon_y}$ (appearing through the SNR parameters, Eq. 4) and their correlation R_{noise} may be approximated from noise recordings. Another constraint is that the division entailed by the renormalization (7) must be well conditioned. This is not the case in the limit of low SNR ($\text{SNR}_x \approx 1$ or $\text{SNR}_y \approx 1$), for small estimation errors in the SNR estimates (4) then translate into large errors in the connectivity estimate (7). Therefore we predict that power bias correction will not be effective when measurement noise dominates.

It is noteworthy that the above considerations directly apply to the neuro-scientifically relevant phase connectivity measure known as coherence (Halliday et al., 1995), as it merely corresponds to a spectrally-resolved version of linear correlation. In this framework, results (6) and (7) hold with correlations (R and R_{noise}) replaced by complex-valued coherency estimates and signal variances (σ^2_x, σ^2_y, $\sigma^2_{\epsilon_x}$, and $\sigma^2_{\epsilon_y}$ appearing in Eq. 4), by power spectral densities. We do not pursue this here and turn to nonlinear amplitude connectivity relevant to the electrophysiological mapping of intrinsic brain networks.

2.2. Co-occurrence of brain rhythms: Amplitude correlation

Assessing the simultaneity of the rise and fall of transient brain oscillations in two brain areas requires first to isolate the amplitude time course of these rhythms and then to assess their temporal covariation.

Isolation of rhythmic activity itself in MEG signals can be performed by band-pass filtering, so we will assume hereafter that x and y correspond to sufficiently narrow-band signals. In this context, x_0 and y_0 represent oscillatory cerebral activity that contains the assumed brain rhythm underlying their functional connection (along with other background neural processes), while ϵ_x and ϵ_y are the band-filtered part of the (possibly wideband) measurement noise. Time-varying oscillatory amplitudes can then be conveniently extracted using the Hilbert transform, which factorizes any band-limited signal, say $x(t)$, as $A_x(t)\,\mathrm{e}^{\mathrm{i}\phi_x(t)}$, where A_x denotes its amplitude time course (a.k.a. Hilbert envelope) and ϕ_x its instantaneous phase time course. (The mathematics of Hilbert transformation is briefly reviewed in the Appendix, section A.1.) This factorization applies to cerebral and noise signals as well, so the relation $x = x_0 + \epsilon_x$ becomes

$$A_x \mathrm{e}^{\mathrm{i}\phi_x} = A_{x_0} \mathrm{e}^{\mathrm{i}\phi_{x_0}} + A_{\epsilon_x} \mathrm{e}^{\mathrm{i}\phi_{\epsilon_x}} \ .$$

The simplest algebraic expression for the amplitude A_x of the measured signal in terms of the amplitude A_{x_0} of the cerebral oscillatory activity and A_{ϵ_x} of the band-filtered noise, is obtained by taking the modulus squared of this equation,

$$A_x^2 = A_{x_0}^2 + A_{\epsilon_x}^2 + 2A_{x_0}A_{\epsilon_x}\cos\left(\phi_{x_0} - \phi_{\epsilon_x}\right) \ . \tag{8}$$

A similar relation holds for the y signals. These expressions will play the same role here as Eq. (2) did in section 2.1.

The temporal dependence of the two oscillatory amplitudes A_x and A_y is conventionally measured as their correlation, i.e., $\mathrm{AEC} = \mathrm{corr}[A_x, A_y]$. Our goal is to express this functional connectivity measure in terms of the neural part $\mathrm{AEC}_0 = \mathrm{corr}[A_{x_0}, A_{y_0}]$ involving only cerebral oscillatory amplitudes A_{x_0} and A_{y_0}, and of a version of the SNR pertaining to the amplitudes that will be identified below. A technical difficulty in this endeavor is that A_x is a nonlinear function of A_{x_0} (see Eq. 8), preventing us to follow the strategy used in section 2.1 for linear correlation. Fortunately, it turns out that the correlation of amplitudes in the AEC can be replaced to a very good approximation by the correlation of amplitudes squared (Wens, 2015), so

$$\mathrm{AEC} \approx \mathrm{corr}[A_x^2, A_y^2] = \frac{\mathrm{cov}(A_x^2, A_y^2)}{\sigma_{A_x^2}\sigma_{A_x^2}} \tag{9}$$

And similarly for AEC_0. The correlation of amplitudes squared is actually closely related to the band-limited power correlation used by de Pasquale and colleagues (de Pasquale et al., 2010; Della Penna et al., 2019), which has been observed to yield the same functional networks as AEC but also quantitatively very similar functional connectivity estimates (Sjøgård et al., 2019). This is an illustration of the validity of this approximation, whose analytical demonstration can be found in Appendix E of Wens (2015).

The line of thoughts followed in section 2.1 for linear correlation can then be applied to the right-hand side of Eq. (9). The situation is fairly similar but somewhat more intricate due to the interplay between amplitude and phase-lag dynamics evidenced by the rightmost term

in the relation (8). We describe below the main results; detailed derivations are relegated to the Appendix (sections A.2 and A.3).

The analog for amplitude squared of the two intermediate results $\mathrm{cov}(x, y) = \mathrm{cov}(x_0, y_0) + \mathrm{cov}(\epsilon_x, \epsilon_y)$ and $\sigma_x^2 = \sigma_{x_0}^2 + \sigma_{\epsilon_x}^2$ of section 2.1 are

$$\mathrm{cov}\left(A_x^2, A_y^2\right) = \mathrm{cov}\left(A_{x_0}^2, A_{y_0}^2\right) + \mathrm{cov}\left(A_{\epsilon_x}^2, A_{\epsilon_y}^2\right) + \mathcal{L}(x, y) + \mathcal{L}(x, \mathrm{H}y) \tag{10}$$

and

$$\sigma_{A_x^2}^2 = \sigma_{A_{x_0}^2}^2 + \sigma_{A_{\epsilon_x}^2}^2 + 2\langle A_x^2\rangle\langle A_{\epsilon_x}^2\rangle - 2\langle A_{\epsilon_x}^2\rangle^2 \,. \tag{11}$$

The main difference with the linear case is the presence of extra terms originating from the interplay between amplitudes and phase lags in Eq. (8). The covariance of amplitude squared (10) receives a contribution

$$\mathcal{L}(x, y) = 8\left[\mathrm{cov}(x, y)\mathrm{cov}(\epsilon_x, \epsilon_y) - \mathrm{cov}(\epsilon_x, \epsilon_y)^2\right] \tag{12}$$

depending on linear covariances between MEG signals x, y and between the corresponding noise signals ϵ_x, ϵ_y, and a similar contribution $\mathcal{L}(x, \mathrm{H}y)$ involving Hilbert transforms $\mathrm{H}y$ and $\mathrm{H}\epsilon_y$. These two terms and the amplitude covariance $\mathrm{cov}\left(A_{\epsilon_x}^2, A_{\epsilon_y}^2\right)$ all depend on noise correlations; they are likely subdominant after leakage correction but we will nevertheless keep track of them as discussed in section 2.1. Further, we show in the Appendix (section A.2) that $\mathcal{L}(x, y)$ turns out to be proportional to the neural zero phase-lag coupling R_0 (and $\mathcal{L}(x, \mathrm{H}y)$ to the neural coupling at $\pi/2$ phase lag). Although R_0 is generally thought to vanish in the resting state, Sjøgård et al. (2019) suggested the existence of spontaneous quasi-zero

lag correlations, at least within the default-mode network. For this reason, we will remain general and retain all contributions in Eq. (10).

The two extra terms in Eq. (11) dictate how to extend the notion (4) of SNR to the case of amplitude squared. Revisiting section 2.1, we can recast Eq. (11) as

$$\frac{1}{\sigma_{A_x^2}^2} = \frac{1}{\sigma_{A_x^2}^2}\left(\frac{\sigma_{A_x^2}^2 - \sigma_{A_{\epsilon_x}^2}^2 - 2\langle A_x^2\rangle\langle A_{\epsilon_x}^2\rangle + 2\langle A_{\epsilon_x}^2\rangle^2}{\sigma_{A_{x_0}^2}^2}\right) = \frac{1}{\sigma_{A_{x_0}^2}^2}\left(1 - \frac{\sigma_{A_{\epsilon_x}^2}^2 + 2\langle A_x^2\rangle\langle A_{\epsilon_x}^2\rangle - 2\langle A_{\epsilon_x}^2\rangle^2}{\sigma_{A_x^2}^2}\right).$$

Comparison with the analogous result $1/\sigma_x^2 = \left(1 - \mathrm{SNR}_x^{-2}\right)/\sigma_{x_0}^2$ suggests to define

$$\mathrm{SNR}_x^{\mathrm{ampl}} = \frac{\sigma_{A_x^2}}{\sqrt{\sigma_{A_{\epsilon_x}^2}^2 + 2\langle A_x^2\rangle\langle A_{\epsilon_x}^2\rangle - 2\langle A_{\epsilon_x}^2\rangle^2}} \tag{13}$$

and likewise for A_y.

Normalizing the covariance (10) of amplitudes squared by their standard deviation and using Eq. (11) and definition (13), leads to our final expression for the AEC (9), i.e.,

$$\mathrm{AEC} = \mathrm{AEC}_0\sqrt{1 - \left(\mathrm{SNR}_x^{\mathrm{ampl}}\right)^{-2}}\sqrt{1 - \left(\mathrm{SNR}_y^{\mathrm{ampl}}\right)^{-2}} + \frac{\mathrm{cov}\left(A_{\epsilon_x}^2, A_{\epsilon_y}^2\right)}{\sigma_{A_x^2}\sigma_{A_y^2}} + \frac{\mathcal{L}(x,y) + \mathcal{L}(x,\mathrm{H}y)}{\sigma_{A_x^2}\sigma_{A_y^2}}. \tag{14}$$

The general discussion that follows Eq. (6) holds without change, and in particular the neural part AEC_0 of amplitude correlation can be recovered via a renormalization procedure

$$\mathrm{AEC}_{\mathrm{ren}} = \frac{\mathrm{AEC} - \frac{\mathrm{cov}\left(A_{\epsilon_x}^2, A_{\epsilon_y}^2\right)}{\sigma_{A_x^2}\sigma_{A_y^2}} - \frac{\mathcal{L}(x,y) + \mathcal{L}(x,\mathrm{H}y)}{\sigma_{A_x^2}\sigma_{A_y^2}}}{\sqrt{1 - \left(\mathrm{SNR}_x^{\mathrm{ampl}}\right)^{-2}}\sqrt{1 - \left(\mathrm{SNR}_y^{\mathrm{ampl}}\right)^{-2}}}. \tag{15}$$

Critically, this quantity is expressed in terms of parameters that are experimentally accessible to MEG recordings. The two subtractive terms in the numerator correct for possible (and likely subdominant) noise correlations and zero phase-lag coupling, and the denominator corrects for the power bias itself.

3. Material and methods

3.1. Synthetic signals for theory validation

To illustrate our main theoretical result and validate the power bias correction method, we simulated pairs of oscillatory signals x and y (playing the role of experimental MEG signals projected at two source locations) with SNR, neural connectivity AEC_0 and noise connectivity $\mathrm{AEC}_{\mathrm{noise}}$ as controlled parameters. To do this, we generated synthetic cerebral signals x_0 and y_0 with varying amplitude correlation AEC_0, as well as noise signals ϵ_x and ϵ_y with varying amplitude correlation $\mathrm{AEC}_{\mathrm{noise}}$, leading to various SNR levels in the synthetic MEG signals x and y. The latter were obtained by summation (2) of cerebral activity and noise. Our main theoretical result (14) was then illustrated by examining the behavior of the AEC estimate as a function of the simulated AEC_0 and SNRs, and the validity of the renormalization procedure (15) for power bias correction by comparing the renormalized estimate $\mathrm{AEC}_{\mathrm{ren}}$ and the simulated AEC_0.

In each simulation, we generated the cerebral signals x_0, y_0 and the noise signals ϵ_x, ϵ_y as four independent realizations of a standard gaussian white noise sampled at 1 kHz for a duration of 5 minutes. These time series were filtered in the α band (8–12 Hz) to simulate

narrow-band oscillatory signals. Of note, the choice of center frequency (here, 10 Hz) merely sets the timescale of the simulations but does not impact results otherwise. Likewise, the choice of bandwidth (here, 4 Hz) does not impact results as long as its ratio to the center frequency remains small enough to successfully extract oscillatory envelopes and phases via Hilbert transformation (see Appendix, section A.1). A correlation between the amplitudes A_{x_0} of x_0 and A_{y_0} of y_0 was then introduced by substituting A_{y_0} with a linear mixture $A_{y_0} + kA_{x_0}$. A fixed value AEC_0 was imposed by setting the mixing coefficient k to

$$k = \frac{\mathrm{AEC}_0}{\sqrt{1 - \mathrm{AEC}_0^2}} \frac{\sigma_{A_{y_0}}}{\sigma_{A_{x_0}}}.$$

A correlation between the amplitudes of the noise signals ϵ_x and ϵ_y was introduced in a similar fashion.

Synthetic MEG signals were finally constructed by summation (2) of these simulated cerebral activity and noise, after independently rescaling both cerebral signals and noise so as to impose fixed values to the SNR parameters (4). Parameters of interest (SNR_x, SNR_y, AEC_0, AEC, and $\mathrm{AEC}_{\mathrm{ren}}$) were estimated from these simulated time courses according to Theory section 2. These simulations were repeated 30 times so as to generate datasets of synthetic functional connectivity and SNR measures commensurate to the experimental resting-state dataset described here below.

3.2. Data acquisition

We investigated the power bias on amplitude connectivity estimated from resting-state MEG recordings of 31 healthy adult volunteers (16 females and 15 males, mean age: 26.4 years, age range: 19–36 years) taken from an existing resting-state dataset used in previous publications (Mary et al., 2015; Vander Ghinst et al., 2016), including functional network mapping (Wens et al., 2014b, 2019). Subjects were all right-handed according to the Edinburgh Handedness Inventory test (Oldfield, 1971), declared no history of neurologic or psychiatric disease, and signed a written informed consent. Usage of these data was conform to the approval emitted by the Ethics Committee of CUB–Hôpital Erasme, where data acquisitions took place.

Neuromagnetic activity was recorded at rest with a 306-channel whole-scalp-covering MEG system (Vectorview Neuromag, Elekta Oy, Helsinki, Finland; now MEGIN) installed in a lightweight magnetically shielded room (Maxshield™, MEGIN; see De Tiège et al., 2008 for its characteristics). Subjects seated comfortably and gazed at a fixation point on the front wall or on a screen during 5 minutes of recording (analog band-pass: 0.1–330 Hz, sampling frequency: 1 kHz). Head movements were tracked online with four head position indicator coils emitting high-frequency localizable magnetic fields. Their location relative to anatomical fiducials as well as more than 150 face and scalp points was determined with an electromagnetic 3D digitizer (Fastrack, Polhemus, Colchester, VT, USA) prior to MEG recording.

An anatomical 3D T1-weighted magnetic resonance image (MRI) of each subject's brain was also acquired after MEG recordings using a 1.5T MRI scanner (Intera, Philips, The Netherlands).

3.3. Preprocessing, filtering and source projection

Environmental magnetic interferences and head movements were suppressed from the resting-state MEG data using the temporal extension of signal space separation (Maxfilter v2.2 with default parameters, MEGIN; see Taulu et al., 2005). Physiological interferences (cardiac activity and eye movements) and system artifacts were further eliminated using an independent component analysis (FastICA, dimension reduction to the first 30 principal components, nonlinear contrast function tanh; see Hyvärinen and Oja, 2000) of MEG signals filtered between 0.5 and 45 Hz (Vigario et al., 2000). Artifactual components were identified through visual inspection and regressed out of the full-rank MEG data. The resulting preprocessed MEG data were finally decomposed spectrally using several band-pass filters into narrow frequency bands (band centers: 1, 2, ..., 45 Hz, bandwidth: 1 Hz).

Source projection was performed using minimum norm estimation (MNE; see Dale and Sereno, 1993). The MEG forward model was computed using a one-layer boundary element algorithm (MNE-C; see Gramfort et al., 2014) based on MRI tissue segmentation (Freesurfer; see Fischl, 2012) and a source grid built from a cubic 5-mm grid in the Montreal Neurological Institute (MNI) template MRI and morphed onto each subject's MRI (non-linear deformation implemented in SPM8; see Friston et al., 2007). The MNE inverse of the forward model was regularized using noise covariance estimated from 5 min-long empty room recordings (with

signal space separation for environmental noise reduction and same narrow-band filters than for resting-state recordings) and a regularization parameter fixed according to a consistency condition (Wens et al., 2015).

3.4. Spectrally-resolved functional connectivity and SNR estimation

Functional connectivity was estimated as the AEC between pairs of source-projected MEG signals x, y according to Theory section 2, with time averages taken over the entire recording duration. Spatial leakage was corrected prior to AEC estimation using a geometric correction (Wens et al., 2015) of spurious functional connectivity due to the spatial blurriness of linear source projection such as MNE (Wens, 2015). Although spatial leakage is inherently symmetrical with MNE (Hauk and Stenroos, 2014), the geometric correction leads to numerical asymmetries. We corrected these asymmetries by averaging the leakage-corrected AEC estimate between x and y and that between y and x. This AEC estimation was performed within each narrow frequency band, allowing examination of functional connectivity spectra.

Following Hipp et al. (2012), we focused first on interhemispheric connections between homologous primary cortices that characterize the sensorimotor network (SMN; MNI coordinates: left node, [−42,−26,54] mm; right node, [38,−32,48] mm), the auditory network (AN; left, [−54,−22,10] mm; right, [52,−24,12] mm), and the visual network (VN; left, [−20,−86,10] mm; right, [16,−80,26] mm). These coordinates were taken from de Pasquale et al., 2012, Hipp et al., 2012. We then considered a functional connectome based on a dense parcellation of the brain into 155 nodes classified in terms of their membership to functional networks according to a fMRI meta-analysis (Della Penna et al., 2019).

To proceed with power bias correction, we further estimated the SNR parameters (4) and (13) at each considered node location. All SNR estimations were applied on source-projected signals and each of their leakage-corrected versions, since both are involved in functional connectivity estimation. The necessary averages involving measurement noise ϵ_x, ϵ_y at these locations were estimated from corresponding empty-room MEG signals. Importantly, source projection and spatial leakage correction of these empty-room data used the exact same forward model and MNE inverse than the resting-state data. This stems from the well-known approach whereby empty-room recordings are used as substitutes for the actual measurement noise occurring during subject's recordings. One caveat with this approximation though, is that a small fraction of SNR estimates (4) turned out close to or lower than the minimal value 1, leading to ill-conditioned or ill-defined renormalization (see discussion below Eq. 7 in section 2.1). In practice, we conservatively excluded any connection for which the SNR estimate (13) at any of its two nodes reached below 1.1 in at least one frequency band. This led to the exclusion of no more than 2% of our individual functional connectivity dataset (spread over 6 out of the 31 subjects).

3.5. Power bias correction

The power bias correction (15) was applied on AEC estimates (prior to node symmetrization) as described in Theory section 2, with x and ϵ_x playing the role of the MEG signal and MEG noise projected at one node, and y and ϵ_y the MEG signal and MEG noise at another node after leakage correction from the location corresponding to x. Symmetrization was then applied as described above to correct for asymmetries induced by leakage correction.

The power bias renormalization factor is nonlinear in the SNR. To examine the importance of this feature, we considered another correction approach based on multiple regression. Regression models are widely used in neuroimaging to discard unwanted effects (covariates of no interest) and highlight effects thought to be relevant (covariates of interest) (Friston et al., 2007). For each connection and each frequency band of our AEC data, we designed the linear model

$$\mathrm{AEC} = \beta_0 + \beta_x \frac{1}{\mathrm{SNR}_x} + \beta_y \frac{1}{\mathrm{SNR}_y} + \beta_\epsilon R_{\mathrm{noise}} + n$$

and determined the coefficients β_0, β_x, β_y, and β_ϵ in a standard manner by minimizing the group variance of the model error n (Friston et al., 2007). To keep the approach generic and independent of the theoretical developments of section 2, we used the basic definition (4) of the SNR rather than the specific form (13) identified in the context of the power bias renormalization (15), and likewise we used the linear noise correlation R_{noise}. Nevertheless, we set the two SNR-related regressors to the inverse SNR as it is reasonable to expect on general grounds that connectivity estimates AEC converge to their true value AEC_0 in the large SNR limit ($\mathrm{SNR}_x \gg 1$ and $\mathrm{SNR}_y \gg 1$). The true value would then be captured by the intercept regressor corresponding to the first term of the above model. More specifically, β_0 would correspond to the group-average of AEC_0, and the error term n to the inter-individual variations.

The regression-based corrected amplitude connectivity estimate can thus be identified as

$$\mathrm{AEC}_{\mathrm{reg}} = \mathrm{AEC} - \beta_x \frac{1}{\mathrm{SNR}_x} - \beta_y \frac{1}{\mathrm{SNR}_y} - \beta_\epsilon R_{\mathrm{noise}} \,. \tag{16}$$

Again, this was applied independently for each pair x, y of source-projected MEG signals (with one being leakage corrected with respect to the other) and within each frequency band, and symmetrization was imposed afterwards.

3.6. Measure statistics of the power bias

We quantified to what extent the power bias affects amplitude connectivity estimation by assessing the relative difference between the measured value AEC and either the ground truth AEC_0 in simulations or the corrected value $\mathrm{AEC}_{\mathrm{ren}}$ in resting-state data.

For the synthetic functional connectivity data, each of the $N_{\mathrm{subj}} = 30$ "subjects" corresponded to a number of simulations where the true connectivity AEC_0 was varied (simulating in a sense spectral variations of connectivity) while the SNR parameters (4) were kept fixed. The power bias measure (PBM) was then taken as

$$\mathrm{PBM} = \frac{\sum_s \left(\langle \mathrm{AEC}^{(s)} \rangle - \langle \mathrm{AEC}_0^{(s)} \rangle \right)^2}{\sum_s \left(\langle \mathrm{AEC}_0^{(s)} \rangle \right)^2} .$$

In this section, brackets $\langle \cdot \rangle$ denote group averaging over N_{subj} subjects (rather than time averaging as in section 2 and Appendix sections A.2 and A.3). Sums run here over all simulations (indexed by superscripts s) performed at fixed SNRs. This PBM index allowed us to quantify the effect of the power bias as a function of SNR; a large PBM indicates a strong effect of the power bias. A closely-related index was also used to estimate the power bias correction error

$$\frac{\sum_s \left(\langle \mathrm{AEC}_{\mathrm{ren}}^{(s)} \rangle - \langle \mathrm{AEC}_0^{(s)} \rangle \right)^2}{\sum_s \left(\langle \mathrm{AEC}_0^{(s)} \rangle \right)^2}$$

as a function of the SNR. A large value of this index indicates poor performance of the correction procedure (15).

For the resting-state MEG connectivity data, the power bias was measured for each connection as

$$\mathrm{PBM} = \frac{\sum_\nu \left(\langle \mathrm{AEC}_{\mathrm{ren}}^{(\nu)} \rangle - \langle \mathrm{AEC}^{(\nu)} \rangle \right)^2}{\sum_\nu \left(\langle \mathrm{AEC}^{(\nu)} \rangle \right)^2},$$

where $\mathrm{AEC}^{(\nu)}$ corresponds to an individual amplitude correlation in the band of center frequency ν. Sums now run over all frequencies ν considered so as to quantify the effect of the power bias on group-averaged AEC spectra. This measure is thus particularly interesting to answer our main question regarding the oscillatory nature of intrinsic functional connectivity. In fact, findings of large PBM would demonstrate substantial modifications of connectivity spectra. The statistical significance of these modifications was established using a version of Hotelling's T^2 test (Hotelling, 1931). Specifically, we computed for each connection the squared Mahalanobis distance in dimension $N_{\mathrm{freq}} = 45$ (corresponding to the number of frequency bands) between connectivity spectra $\mathrm{AEC}^{(\nu)}$ before correction and $\mathrm{AEC}_{\mathrm{ren}}^{(\nu)}$ after correction, under the multivariate null hypothesis $\langle \mathrm{AEC}_{\mathrm{ren}}^{(\nu)} - \mathrm{AEC}^{(\nu)} \rangle = 0$ that the power bias does not affect AEC estimation. One issue in this computation is the non-invertibility of the corresponding $N_{\mathrm{freq}} \times N_{\mathrm{freq}}$ sample covariance matrix, as the natural bandwidth of neurophysiological processes leads to inter-dependent frequencies. For this

reason, the covariance was pseudo-inverted using its first D largest eigenvalues. The number D of effectively independent frequencies was taken as the minimum number of eigenvalues summing up to 99% of the total variance. Statistical inference was then performed at significance level $p < 0.05$ using Hotelling's $T^2_{D,N_{\text{subj}}-1}$ distribution in dimension D with $N_{\text{subj}} - 1$ degrees of freedom. Of notice, N_{subj} was slightly smaller than the total number of subjects (31) for a few, sparsely distributed connections due to the technical caveat mentioned at the end of section 3.4. The false positive rate in the resting-state functional connectome was controlled by Bonferroni correction for the number of effectively independent connections (Sjøgård et al., 2019) estimated as $\rho(\rho - 1)/2$, where ρ denotes the rank of the MEG forward model restricted to the nodes of the connectome (Wens et al., 2015). The same approach was used to measure and assess statistically the impact of the multiple regression (16) on AEC spectra.

Finally, given that the correction procedure (15) controls for noise correlations and linear synchronization on top of the power bias, we further assessed the relative impact of the noise term

$$t_{\text{noise}} = \frac{\dfrac{\operatorname{cov}\left(A^2_{\epsilon_x}, A^2_{\epsilon_y}\right)}{\sigma_{A^2_x}\sigma_{A^2_y}}}{\sqrt{1 - \left(\text{SNR}^{\text{ampl}}_x\right)^{-2}}\sqrt{1 - \left(\text{SNR}^{\text{ampl}}_y\right)^{-2}}}$$

and of the synchronization term

$$t_{\text{sync}} = \frac{\dfrac{\mathcal{L}(x, y) + \mathcal{L}(x, \text{H}y)}{\sigma_{A^2_x}\sigma_{A^2_y}}}{\sqrt{1 - \left(\text{SNR}^{\text{ampl}}_x\right)^{-2}}\sqrt{1 - \left(\text{SNR}^{\text{ampl}}_y\right)^{-2}}}$$

compared to the main power bias correction term

$$t_{\text{power bias}} = \frac{\text{AEC}}{\sqrt{1-\left(\text{SNR}_x^{\text{ampl}}\right)^{-2}}\sqrt{1-\left(\text{SNR}_y^{\text{ampl}}\right)^{-2}}}.$$

Each of these terms were estimated from resting-state MEG data separately for each subject, connection and frequency ν, and the relative contributions of noise correlations and linear synchronization were then measured as

$$\alpha_{\text{noise}} = \frac{\sum_\nu \langle t_{\text{noise}}^{(\nu)} \rangle^2}{\sum_\nu \langle t_{\text{power bias}}^{(\nu)} \rangle^2}, \qquad \alpha_{\text{sync}} = \frac{\sum_\nu \langle t_{\text{sync}}^{(\nu)} \rangle^2}{\sum_\nu \langle t_{\text{power bias}}^{(\nu)} \rangle^2}.$$

3.7. Data and code availability statement

Data and code will be made available upon reasonable request to the corresponding author and with the approval of institutional authorities (CUB – Hôpital Erasme and Université libre de Bruxelles).

4. Results

4.1. Theory validation on synthetic signals

Our main theoretical result (14) provides an analytical description of the power bias in AEC. We illustrate the most salient features in Fig. 1 using synthetic signals simulated at various SNR levels. We started with simulations based on uncorrelated noise in order to isolate the power bias itself from the effect of noise correlation (Fig. 1a–c). Figure 1(a) shows that AEC

depends linearly on the simulated neural connectivity (ground truth AEC_0), with a slope that decreases as the SNR gets lower. The slope is close to one at high SNR, indicating accurate AEC estimation ($AEC \approx AEC_0$, see curve at SNR = 5.10 in Fig. 1a); but then it decreases as the SNR gets lower, revealing functional connectivity underestimation. This SNR-dependent underestimation corresponds precisely to the power bias. Plotting the slope against the SNR at one node illustrates the nonlinearity of the power bias in the SNR (Fig. 1b). It raises sharply from zero at small SNR (i.e., connectivity is undetected when noise dominates the signal) and plateaus at large SNR (connectivity is detected but is still underestimated). This plateau further depends on the SNR at the other node and approaches the maximal value 1 (unbiased estimation of neural connectivity) at large SNR. Technically, Fig. 1(b) illustrates nonlinearity in the amplitude-specific SNR measure (13) rather than the classical SNR measure (4); however that does not change our discussion because they turned out proportional to each other (Fig. 1c).

To illustrate the effect of noise correlations on AEC estimation, we generated synthetic functional connectivity data that incorporate correlated noise in the absence of genuine connectivity (ground truth: $AEC_0 = 0$). Figure 1(d) indicates a linear relationship between AEC estimates and noise amplitude connectivity with a SNR-dependent slope, in line with Eq. (14). Noise correlation leads to fairly limited AEC overestimation at SNRs above 2; but this effect increases substantially as the SNR decreases down to 1.

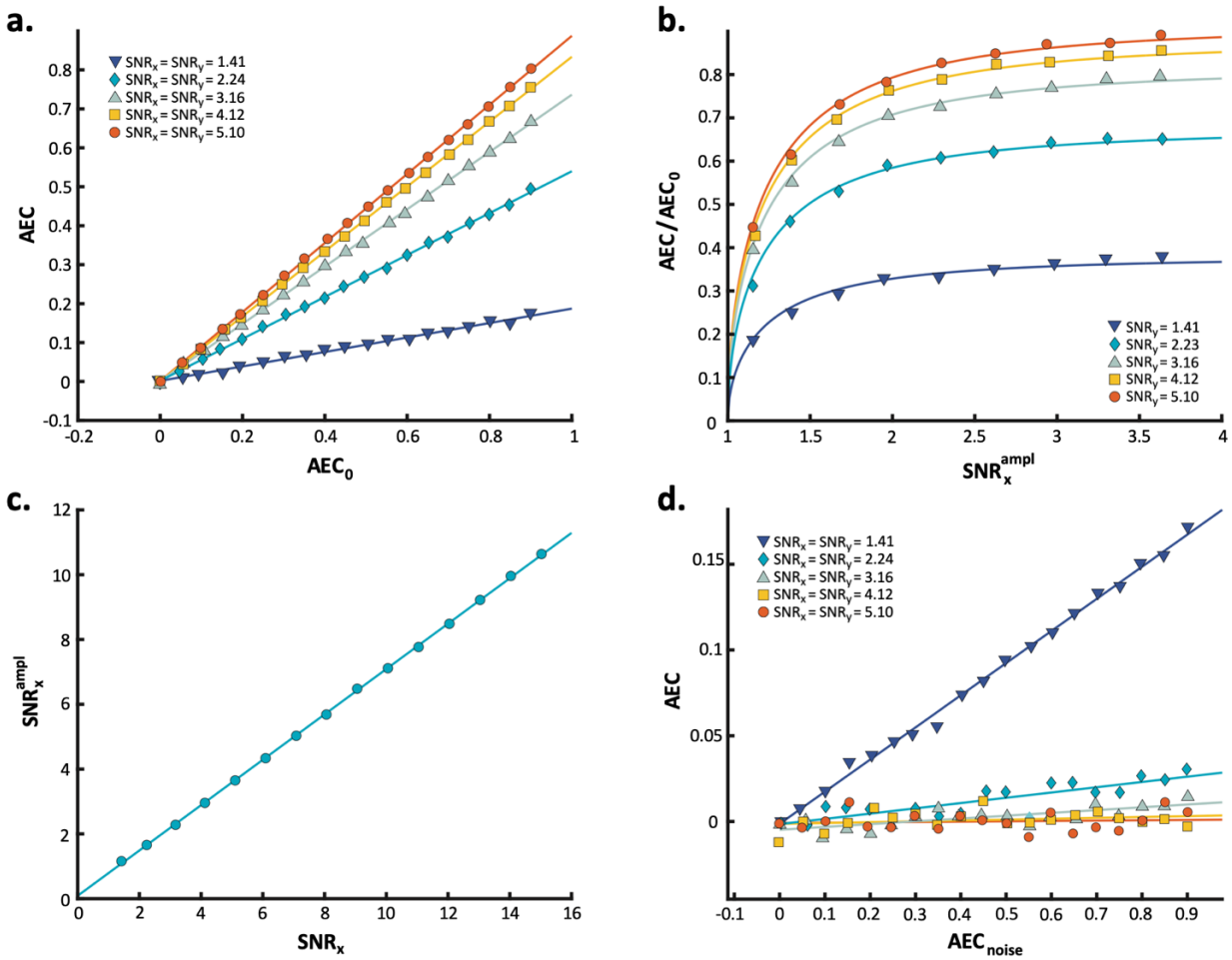

Figure 1: Illustration of the power bias in amplitude correlation. Pairs of synthetic MEG signals (x, y) were simulated at various SNR levels with neural functional connectivity and without noise correlation (panels a–c), and with noise correlation and without neural functional connectivity (panel d). (a) Linear relationship between AEC estimation and simulated ground truth AEC_0. (b) Nonlinear SNR dependence of the power bias, illustrated by plotting the slope (AEC/AEC_0) as a function of the amplitude-specific SNR measure (SNR^{ampl}, Eq. 14). (c) Linear relationship between SNR^{ampl} and the classical SNR measure (4). (d) Linearity of AEC estimation in noise amplitude connectivity (AEC_{noise}). Model curves are superimposed to data points (panels a, c, d, linear regression; panel b, nonlinearity $\left(1-\left(SNR^{ampl}\right)^{-2}\right)^{1/2}$).

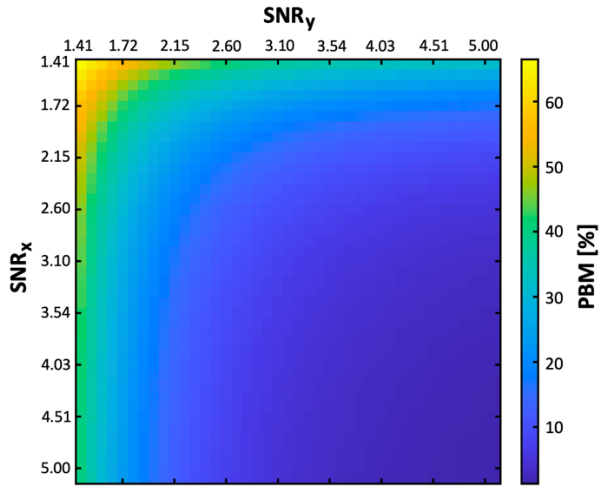

Figure 2: Measurement of the power bias in amplitude correlation. Synthetic functional connectivity data were simulated (without noise correlation) while varying systematically node SNRs. The deviation of AEC estimates from the simulated neural connectivity is quantified using the PBM index (section 3.6). The PBM is plotted against the SNR measure (4) at the two nodes.

We supplemented the above qualitative data with a quantitative assessment of the effect size of the AEC power bias in simulations where both node SNRs are varied systematically. We used the PBM index for that purpose, as it measures to what extent AEC deviates from the simulated ground truth. The deviation was about 60% when the two nodes exhibited low SNR of 1.4, and decreased rapidly at higher SNRs to reach below 10% when both node SNRs are above 3 (Fig. 2). We conclude that the impact of the power bias should be fairly limited in situations where the SNR exceeds 3.

Finally, we sought to assess the validity of our power bias correction method (15) based on the renormalization procedure (Fig. 3). Figure 3(a) shows that the correction allows to recover successfully the simulated neural functional connectivity (compare to the

uncorrected case, Fig. 1a). The correction showed high performance, even at the lowest SNRs simulated (0.4% correction error at SNR = 1.4), and got even better at larger SNRs. This provides proof of concept for our power bias correction.

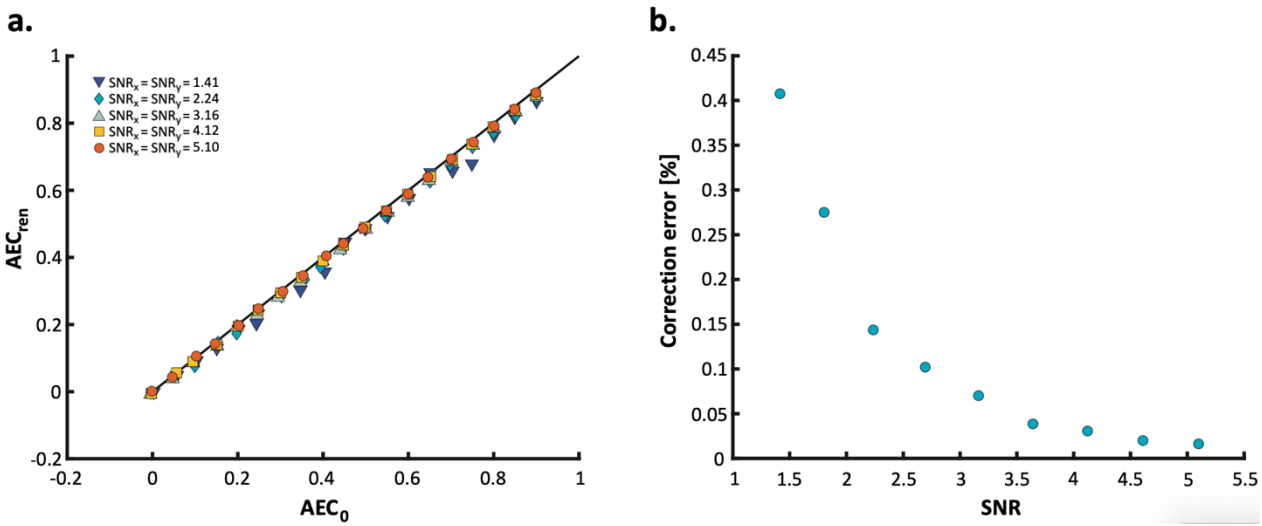

Figure 3: Efficiency of the power bias correction in amplitude correlation. Pairs of synthetic MEG signals (x, y) were simulated at various SNR levels with neural functional connectivity and without noise correlation. (a) Corrected connectivity (AEC_{ren}) plotted as function of the simulated ground truth AEC_0. The black diagonal line indicates perfect correction (i.e., $AEC_{ren} = AEC_0$). (b) Correction error measuring the deviation between corrected (AEC_{ren}) and simulated (AEC_0) connectivity (section 3.6).

4.2. Power bias in interhemispheric connectivity of bilateral functional networks

The correction method being validated, we investigated the impact of the power bias on intrinsic functional connectivity by comparing AEC estimation at rest with and without power bias. We focused first on the interhemispheric connection of three primary brain networks (Fig. 4). All uncorrected AEC spectra (Fig. 4, top, blue) exhibited typical peaks in

the α and the β frequency bands. These connectivity peaks coincide with the presence of rhythmic brain activity at the corresponding nodes, as may be seen from SNR spectra (Fig. 4, bottom). Power bias correction did not modify these connectivity spectra (Fig. 4, top, red) and was associated with a small effect size (PBM $= 1\%$ for all three connections). That is due to the observation of consistently large SNR in MEG resting-state signals over a wide frequency range. Node SNR exceeded 3 (for which simulations predicted PBM below 10%, see Fig. 2) from low frequency up to about 30 Hz, and could reach up to the value 16 (for which simulations predict PBM well below 1%) in the α band. The mere 1% effect of the power bias on interhemispheric connectivity spectra thus reflects this mixture of high to very high SNR over the frequency spectrum. Accordingly, the largest effect arose at high frequency (30–45 Hz) precisely where the SNR is least (between 2 and 3), as may be expected from Fig. 2. Statistical analysis revealed that the small effect of the power bias on interhemispheric functional connectivity spectra is marginally significant (SMN, $p = 0.007$; AN, $p = 0.053$; VN, $p = 0.025$).

To assess the importance of SNR nonlinearity in power bias correction, we used linear regression of node SNRs (and of noise correlation; see section 3.5) as an alternative correction approach. This led to a strong, highly significant deformation of functional connectivity spectra (Fig. 4, top, yellow; SMN, PBM $= 110\%$, $p = 2.10^{-6}$; AN, PBM $= 550\%$, $p = 2.10^{-6}$; VN, PBM $= 130\%$, $p = 8.10^{-8}$). Even though the original peaks can be somewhat identified, the resulting AEC spectra appeared much more erratic (especially in AN). This suggests that linear regression is inadequate for power bias correction, and that taking into account the nonlinearity shown in Fig. 1(b) is fundamental. We illustrate this point further in Fig. 5, where we compare the nonlinear power bias model and the linear

regression model from the SMN connectivity data at 9 Hz. The regression surface corresponds to a flat plane whose intercept value (i.e., the linear extrapolation of AEC to very large SNR values, $\mathrm{SNR}_x^{-1} = \mathrm{SNR}_y^{-1} = 0$, where power should not bias functional connectivity) yields the corrected AEC. By contrast, the nonlinearity of our power bias model (Eq. 14, Figs. 1b and 2) yields a curved surface that flattens when approaching the intercept, which led to a lower renormalized AEC. This nonlinear flattening of the power bias actually explains why the linear regression tends to overestimate AEC in Fig. 4.

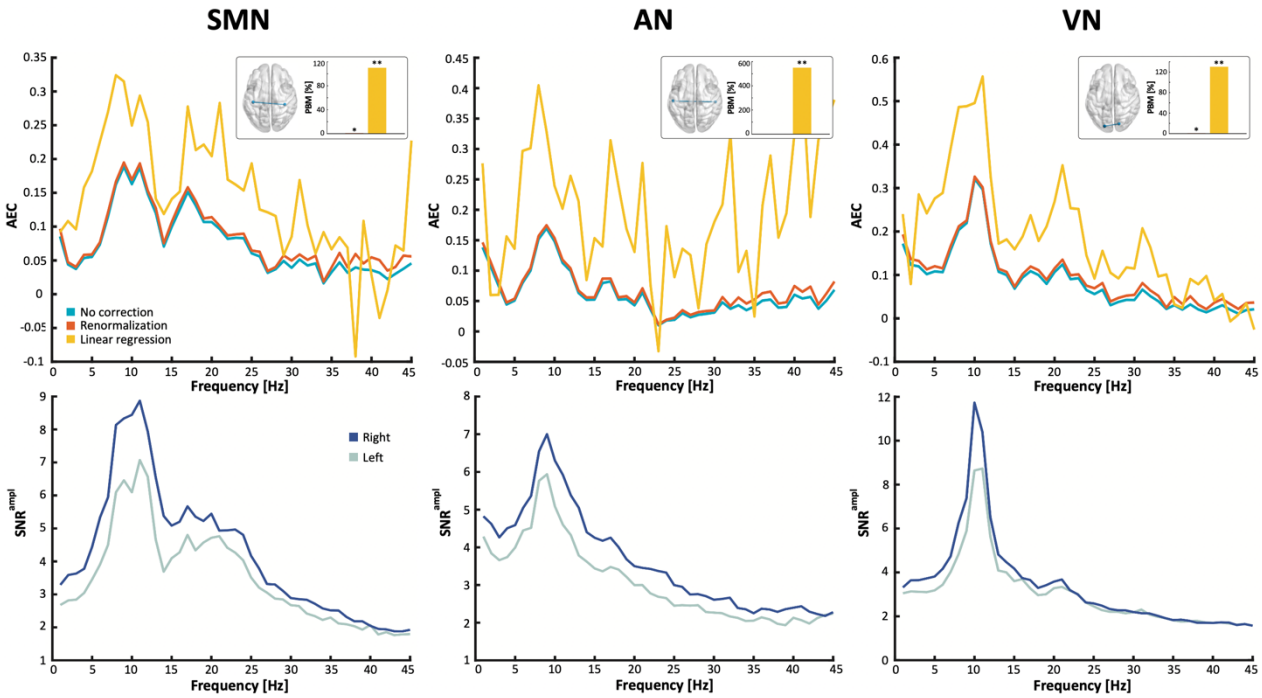

Figure 4: Power bias correction in interhemispheric amplitude correlation spectra. Top. Spectrally-resolved AEC are shown for three interhemispheric functional connections (shown in inserts) without correction (blue), after power bias correction based on AEC renormalization (red), and after regression (yellow). Inserts show the corresponding connection on the MNI glass brain and compare the PBM index associated with each correction (i.e., a measure of the spectral deformation of connectivity; *, $p < 0.05$, **, $p < 5.10^{-3}$). **Bottom.** Spectral decomposition of the amplitude-specific SNR measure (13) at the two nodes of each connection.

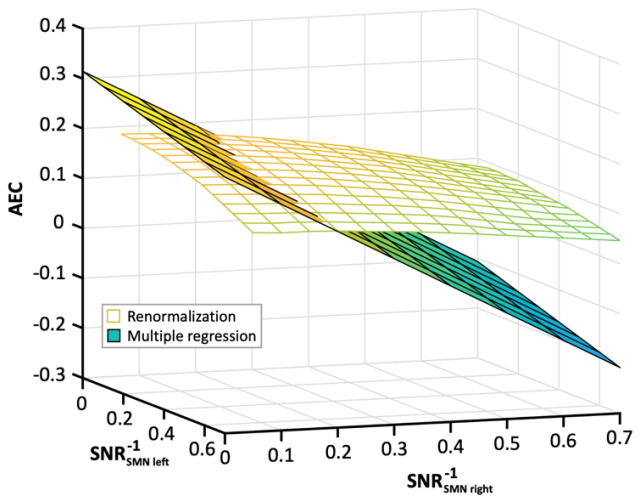

Figure 5: Comparison of power bias correction and multiple regression. This example taken from the resting-state SMN connectivity data at 9 Hz shows two model surfaces used for two distinct correction methods. The planar surface corresponds to multiple regression and the curved one, to power bias correction by AEC renormalization (15). In both cases, correction consists in extrapolating AEC to the intercept value above $\mathrm{SNR}_x^{-1} = \mathrm{SNR}_y^{-1} = 0$.

4.3. Power bias in the functional connectome

Our observations at the level of interhemispheric functional connectivity generalized to the connectome level. The PBM index revealed a consistently small impact of the power bias that was not statistically significant across the whole functional connectome (Fig. 6, left). The strongest effect corresponded to a 12% change at a connection linking the ventral attentional network (node MNI coordinates, [12, 5, 61] mm) and the visual network ([−31, −77, -17] mm). Further inspection of this worst-case example (Fig. 6, right) shows that the connectivity spectrum indeed remained similar after correction. We conclude that the power bias does not impact intrinsic functional connectivity at rest nor its spectral features.

We further used these functional connectome data to explore a couple of methodological questions about power bias correction. First, Fig. 7 confirms the inadequacy of the linear regression at the connectome level (compare PBM scales in Figs. 6 and 7, left), as it strongly and significantly deformed amplitude connectivity spectra everywhere. Second and finally, given that our correction method (15) not only controls for the power bias but also for noise correlation and spontaneous linear synchronization, we assessed the contribution of the two latter factors relative to that of the power bias *per se* (Fig. 8). Noise correlation amounted to less than 0.1% of the power bias, as was expected based on the fact that connectivity data were obtained after spatial leakage correction. The contribution of linear synchronization was slightly larger but still highly subdominant ($\alpha_{\text{sync}} < 1.7\%$).

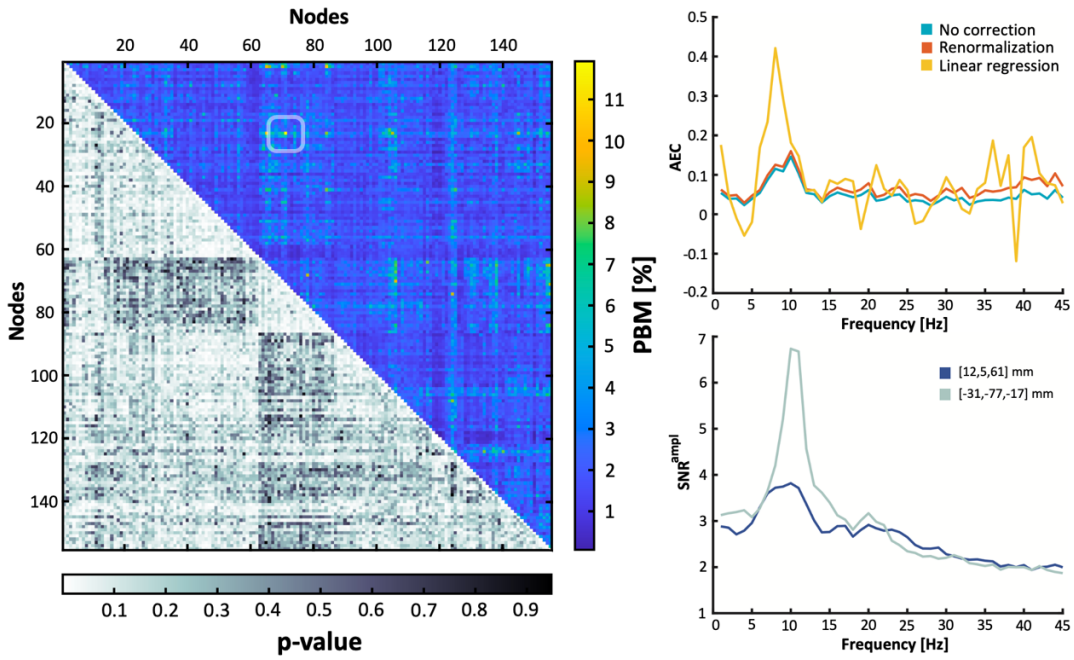

Figure 6: Power bias in amplitude correlation spectra of the connectome. Left. The effect of power bias correction on AEC spectra was mapped using the PBM across the 155-node connectome, arranged as an upper-right triangular matrix. The lower left triangle shows the uncorrected p-value of the corresponding statistic (Hotelling T^2 test). The significance level controlling for the false positive rate across the connectome

corresponds to $p = 3 \times 10^{-5}$. **Right.** Functional connectivity (top) and power (bottom) spectra of the connection exhibiting maximal PBM. Its location in the connectome is highlighted in the left panel.

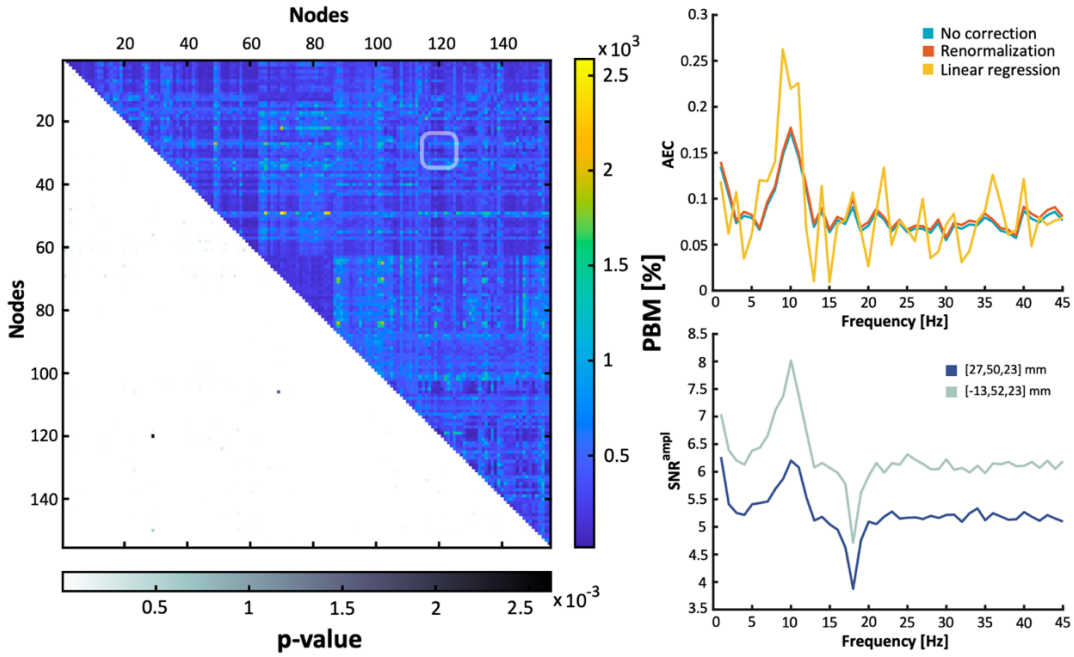

Figure 7: Power bias correction via linear regression in amplitude correlation spectra of the connectome. All is as in Fig. 6, except that the highlighted connection corresponds to the least amount of correction.

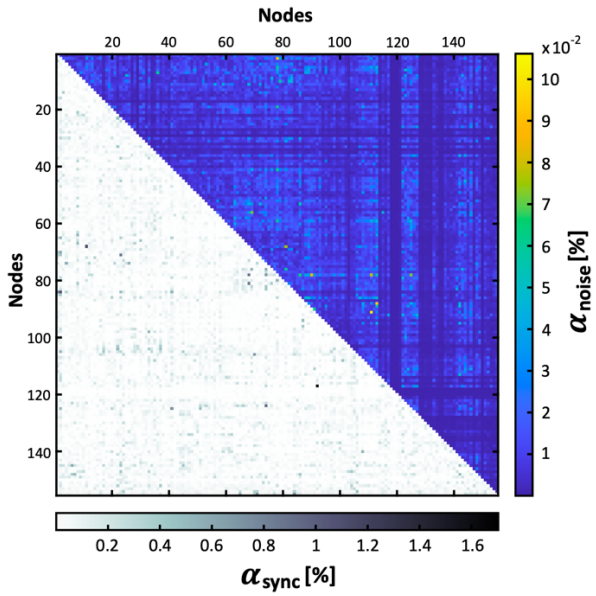

Figure 8: Relative contribution of correction features. The impact of noise correlation (α_{noise}) and linear synchronization (α_{sync}) is mapped across the 155-node connectome. See section 3.6 for precise definitions.

5. Discussion

Our analysis demonstrated that the power bias can be successfully corrected using a nonlinear renormalization procedure derived from proper theoretical analysis, but not using classical multiple regression. Investigation of resting-state MEG revealed that the power bias has a fairly limited impact on frequency-dependent AEC connectome estimation, thanks to the high SNR of MEG recordings even at rest. Beyond methodological aspects, this provides direct empirical confirmation that intrinsic functional connectivity based on resting-state AEC does reflect, from an electrophysiological standpoint, couplings among spontaneous brain rhythms.

5.1. Intrinsic functional networks reflect interacting brain rhythms

The oscillatory nature of intrinsic functional connectivity at rest was taken for granted since the first successful electrophysiological mappings of spectrally-resolved brain networks with MEG (Brookes et al., 2011; Hipp et al., 2012), and was actually considered even before (Leopold et al., 2003). Still, the effect of the power bias (Muthukumaraswamy and Singh, 2011) was not controlled explicitly, leaving the door open that functional connectivity may not be specific to rhythmic activity (Hipp and Siegel, 2015). The main neuroscientific conclusion of our analysis is that intrinsic functional networks do indeed correspond to interacting neural oscillations.

This experimental evidence confirms the consensus on what are the neurophysiological mechanisms of intrinsic functional connectivity revealed by resting-state AEC analysis (Cabral et al., 2014a; Deco et al., 2011). Large-scale neurocomputational models seeking to describe the underlying biophysics often share the same spirit (notwithstanding differences in their details). They start with local high-frequency oscillations, typically in the γ band, generated within each isolated neural population, e.g., through feedback loops between excitatory and inhibitory neurons (Wilson and Cowan, 1972). These fast, local oscillations then interact via long-range excitatory synaptic couplings supported by the anatomical circuitry that connects remote populations. This results into a collective, brain-wide dynamics from which network-level brain rhythms unfold at lower frequencies, mostly in the θ, α and β bands due to conduction delays (Cabral et al., 2014b, 2017; Tewarie et al., 2019). In this framework, functional connectivity is thus an emergent dynamical phenomenon that can be described in terms of interacting neural oscillations. The significance of our data is to

set this theoretical framework on firmer grounds. Large-scale neurocomputational models scarcely generate these local cortical oscillations but rather use them as a starting point, either by modeling neural populations explicitly as oscillators with Kuramoto-like models (Breakspear et al., 2010; Cabral et al., 2011, 2014b), or as neural mass models with parameters chosen to exhibit a limit cycle or at least to stand at the brink of its bifurcation (Deco et al., 2009; Tewarie et al., 2019; Wilson and Cowan, 1972). Admittedly, population-level oscillations are generically observed in local, fully connected networks of spiking neurons (Gerstner et al., 1996); still other possibilities involving irregular, chaotic behavior have been described in local networks exhibiting excitation-inhibition balance (Brunel, 2000; Brunel and Wang, 2003; van Vreeswijk and Sompolinsky, 1996). Had power bias correction demonstrated a broadband functional connectivity, the latter possibility could have been reconsidered. In fact, chaotic or stochastically-driven models have been used in the context of fMRI connectivity (Deco et al., 2009; Honey et al., 2007), but to our knowledge their consequence at the level of MEG connectivity has not been investigated. Our main result provides independent empirical data that such revision is, fortunately, not warranted. The conceptual framework based on the interplay between locally generated cortical oscillations and large-scale delayed interactions, thus stands.

The lack of impact of the power bias should not be overinterpreted as indicating a complete absence of relationship between oscillatory power and functional connectivity. The power bias only concerns the non-physiological contribution of power to functional connectivity estimation through the SNR. A physiological relationship is on the other hand not only possible but plausible. If a functional network emerges from a distributed brain rhythm in a specific frequency range, the areas making up this network must involve this rhythm and

thus exhibit high oscillatory power in this frequency range. This is presumably the simple reason for the coincidence of power and connectivity spectra (see Figs. 4 and 6). Realizing that this coincidence is physiological and not artifactual, allows to understand why the broadband functional connectivity hypothesis of Hipp and Siegel (2015) may not be warranted after all. This hypothesis was based on the assumption that spectral similarities between reliability measures of functional connectivity estimation and SNR are the result of an artifact (i.e., the power bias), but our data suggest that they do reflect physiology. Beyond that, our analysis does not further inform us on the nature of the physiological relationship between power and functional connectivity. Daffertshofer and van Wijk (2011) demonstrated explicitly how local oscillatory power may influence long-range synchronization through a purely neurodynamical mechanism. This was also illustrated by Tewarie et al. (2018) using simulated biophysical models. Interestingly, the latter work included discussion of the power bias in MEG connectivity; the authors argued that the relationship observed between power and phase couplings in MEG data is physiological because models do exhibit such relationship. A direct proof of this claim can actually be devised based on proper power bias correction of phase connectivity along the lines suggested at the end of section 2.1 (data not shown). An interesting avenue for future works is to interpret rigorously findings of transient phase couplings based on time-embedded hidden Markov modeling of resting-state MEG recordings, which is partially confounded by power (Vidaurre et al., 2018).

5.2. Power bias correction is not fundamental to amplitude connectivity analysis

Our conclusion regarding the neurophysiology of intrinsic functional connectivity at rest stands upon a rigorous approach to power bias correction of AEC, which warrants discussion of a few methodological points.

Our theoretical analysis of the power bias in AEC was based on two approximations that were necessary to carry out analytical developments. First, we relied heavily on the machinery of the Hilbert transform in the limit of narrow-band signals, which guarantees a gap in timescales between fast oscillatory phases and slow modulatory amplitudes (see Appendix sections A.1 and A.2). However, this limit does not entail any neurophysiological assumption and was merely ensured by appropriate narrow-band filtering. Second, we replaced the AEC by the correlation between oscillatory power, i.e., amplitude squared (see Eq. 9), but this replacement has little effects on amplitude connectivity estimation (Wens, 2015). Our validation of the main theoretical result (14) with synthetic data actually establishes the accuracy of both approximations. It is noteworthy that the second approximation (9) could have been avoided altogether, had we measured intrinsic functional connectivity with power correlation from the start. We did not do so here to keep in line with a large portion of the literature on MEG amplitude connectivity. Beyond that, our model of the power bias did not require any further assumption, except for the fairly reasonable fact that brain activity is temporally independent from MEG measurement noise. The price to pay for this degree of generality was to slightly overcomplicate the main result (14) by keeping track of the possible contribution of noise correlations. This is a different effect than the power bias itself, which corresponds to the SNR-related underestimation of neural functional connectivity (see

discussion below Eq. 6). This underestimation effect is actually fairly intuitive. Low SNR implies a higher proportion of random noise in measurements, which in turn decreases correlation estimates; reliable correlation estimation is recovered at high enough SNR. The latter case appears to be the rule in MEG recordings, at least at rest in physiological condition. This means that power bias correction will probably not appear as an absolute requisite for investigations of AEC-based functional connectivity. Still, it is noteworthy that our analytical developments were needed to demonstrate this non-trivial claim (Muthukumaraswamy and Singh, 2011; Tewarie et al., 2018).

This being said, systematic usage of power bias correction may represent the safest course of action in future functional connectivity studies. Its impact may be typically limited when the SNR remains large enough in all conditions considered, but we cannot exclude specific situations where brain rhythms would be suppressed to the point that power bias becomes relevant. Possibilities include, e.g., task-induced desynchronizations (Pfurtscheller and Lopes da Silva, 1999), pharmacological treatments (Leong et al., 2022), and brain pathologies (Babiloni et al., 2021). We should keep in mind though that our correction cannot handle the limit SNR $\rightarrow 1$ where brain rhythms are completely suppressed, due to an instability of the renormalization (15); but then the very notion of neural functional connectivity loses meaning in this limit. It may thus be useful in practice to precede functional connectivity analysis with a qualitative check of oscillatory power and exclude such extreme cases. This also prompts the question of whether better alternatives would exist for a systematic correction of the power bias. We included here a comparison to a regression model, which proved inadequate due to the inherent nonlinearity of the power bias. This regression model is closely related to a within-condition power regression of functional connectivity data,

which in our experience tends to spuriously exacerbate connectivity differences across two conditions (unpublished data). That is why in past publications, we relied on regression designs that suppress specifically the effect of between-condition power changes in corresponding connectivity differences (Naeije et al., 2019; Sjøgård et al., 2020; Van Dyck et al., 2021a). Our present analysis demonstrates the usefulness of moving away from generic linear modeling and towards methodological developments that integrate neurophysiological data and physically motivated models of brain dynamics.

Author contribution

A.C. and V.W. designed study; A.M., M.V.G., and V.W. acquired data; A.C. and V.W. developed theory; A.C. contributed to analytical tools; A.C., X.D.T. and V.W. analysed data; A.C., A.M., M.V.G., S.G., X.D.T., and V.W. wrote and reviewed manuscript.

Additional information

Declarations of interest: none

Acknowledgements

X.D.T. is Clinical Researcher at the Fonds de la Recherche Scientifique (F.R.S.–FNRS, Brussels, Belgium). A.M. (Postdoctoral Researcher) is supported by the F.R.S.-FNRS (grant reference 1226419F). The authors acknowledge support from the F.R.S.–FNRS (research convention Excellence of Science EOS MEMODYN, 30446199). The MEG project at the CUB–Hôpital Erasme is financially supported by the Fonds Erasme (Research Convention "Les Voies du Savoir", Brussels, Belgium).

Appendix A

We derive here Eqs. (10) and (11) that underlie our main theoretical result (14) about the AEC. We start by reviewing some background about the Hilbert transform (section A.1) in order to justify several technical identities (section A.2) needed for the derivation itself (section A.3).

A.1. Separation of timescales in oscillatory dynamics

We consider a general signal $x(t)$, whose Fourier spectrum $\hat{x}$ is supported on a frequency band of center ν_0 and half-width $\Delta\nu < \nu_0$. Such signal can be factorized according to

$$x(t) = A_x(t) \cos \phi_x(t) \ , \tag{A1}$$

where the amplitude A_x and phase ϕ_x are determined through the relationship

$$A_x(t)\, \mathrm{e}^{\mathrm{i}\phi_x(t)} = \int_{\nu_0-\Delta\nu}^{\nu_0+\Delta\nu} \hat{x}(\nu)\, \mathrm{e}^{2\pi \mathrm{i}\nu t}\, \mathrm{d}\nu \ . \tag{A2}$$

The Hilbert transform Hx corresponds to the signal (A1) but with 90-degree lagged phase $\phi_x(t) - \pi/2$, i.e.,

$$\mathrm{H}x(t) = A_x(t) \sin \phi_x(t) \ . \tag{A3}$$

In the narrow-band limit $\Delta\nu \ll \nu_0$ pertaining to oscillatory dynamics, A_x captures slow modulations of the amplitude and ϕ_x rapid phase oscillations at an instantaneous frequency that varies slowly around the center frequency ν_0. A succinct way to understand this basic property is to apply a change of variable $\nu \longrightarrow \nu_0 + \nu$ in the Fourier integral (A2), which yields

$$A_x(t)\,\mathrm{e}^{\mathrm{i}\phi_x(t)} = \mathrm{e}^{2\pi\mathrm{i}\nu_0 t}\int_{-\Delta\nu}^{\Delta\nu}\hat{x}(\nu_0+\nu)\,\mathrm{e}^{2\pi\mathrm{i}\nu t}\,\mathrm{d}\nu\ .$$

The integral in the right-hand side determines a complex-valued signal $A_x(t)\,\mathrm{e}^{\mathrm{i}\delta_x(t)}$ with same amplitude than x, a phase $\delta_x = \phi_x - 2\pi\nu_0 t$ that corresponds to the phase shift between x and the carrying oscillation at frequency ν_0, and a Fourier spectrum restricted to frequencies below $\Delta\nu$. This implies that the amplitude A_x and the phase shift δ_x both evolve on timescales much slower than the carrying oscillation.

A.2. Technical identities on time averages

This separation of timescales applies to any narrow-band signal; in our setup x may be any one of the cerebral signals x_0, y_0 or measurement noises ϵ_x, ϵ_y. Together with the assumption that cerebral activity and noise are temporally independent, this is key to estimate analytically the several time averages that originate from the last term in Eq. (8).

While evaluating the correlation of amplitudes squared (9), a number of simplifications emerge from identities of the form

$$\langle A_{x_0}^a A_{\epsilon_x}^b A_{y_0}^c A_{\epsilon_y}^d \cos\left(\phi_{x_0} - \phi_{\epsilon_x}\right)\rangle = 0 \qquad (A4)$$

holding for any non-negative integers $a, b, c, d \geq 0$, and similar identities involving the phase lag $\phi_{y_0} - \phi_{\epsilon_y}$. To demonstrate Eq. (A4), we expand the left-hand side with a classical trigonometric identity, apply the independence of x_0, y_0 and ϵ_x, ϵ_y to factorize time averages, and thus obtain

$$\langle A_{x_0}^a A_{y_0}^c \cos\phi_{x_0}\rangle\,\langle A_{\epsilon_x}^b A_{\epsilon_y}^d \cos\phi_{\epsilon_x}\rangle + \langle A_{x_0}^a A_{y_0}^c \sin\phi_{x_0}\rangle\,\langle A_{\epsilon_x}^b A_{\epsilon_y}^d \sin\phi_{\epsilon_x}\rangle\ .$$

Each factor in this expression vanishes because amplitudes remain approximately constant over any cycle of the phase oscillations. Let us consider for instance the first factor; inserting $\phi_{x_0} = 2\pi\nu_0 t + \delta_{x_0}$ yields

$$\langle A_{x_0}^a A_{y_0}^c \cos\phi_{x_0}\rangle = \langle A_{x_0}^a A_{y_0}^c \cos\delta_{x_0} \cos(2\pi\nu_0 t)\rangle - \langle A_{x_0}^a A_{y_0}^c \sin\delta_{x_0} \sin(2\pi\nu_0 t)\rangle \,.$$

The Riemann-Lebesgue lemma establishes that each of these two terms vanish in the limit $\nu_0/\Delta\nu \to \infty$, but this formal argument can be explained on the basis of the separation of timescales. Slow amplitude and phase modulations involve frequencies below $\Delta\nu \ll \nu_0$ and so they are constant over short time periods corresponding to one cycle of the rapid carrying oscillation at frequency ν_0. This allows to factorize time averages into fast oscillatory averages over one cycle and slow modulatory averages over long times, e.g.,

$$\langle A_{x_0}^a A_{y_0}^c \cos\phi_{x_0}\rangle \approx \langle A_{x_0}^a A_{y_0}^c \cos\delta_{x_0}\rangle\langle\cos(2\pi\nu_0 t)\rangle - \langle A_{x_0}^a A_{y_0}^c \sin\delta_{x_0}\rangle\langle\sin(2\pi\nu_0 t)\rangle \,.$$

This expression vanishes since $\langle\cos(2\pi\nu_0 t)\rangle = \langle\sin(2\pi\nu_0 t)\rangle = 0$ over any cycle. The same holds for all terms encountered above. This ends the demonstration of the identities (A4).

We will also encounter non-vanishing averages involving second powers of cosines. First,

$$\langle A_{x_0}^2 A_{\epsilon_x}^2 \cos\left(\phi_{x_0} - \phi_{\epsilon_x}\right)^2\rangle = \frac{\langle A_{x_0}^2\rangle\langle A_{\epsilon_x}^2\rangle}{2} \qquad (A5)$$

and likewise for the y signals. To derive this identity, we again use trigonometry to rewrite the left-hand side as $\langle A_{x_0}^2 A_{\epsilon_x}^2\left[1 + \cos 2\left(\phi_{x_0} - \phi_{\epsilon_x}\right)\right]/2\rangle$. The cosine term vanishes for the exact same reasons than Eq. (A4) holds, leaving $\langle A_{x_0}^2 A_{\epsilon_x}^2\rangle/2$. The latter average factorizes since cerebral activity and noise are independent, leading us back to Eq. (A5).

The second non-vanishing identity is

$$\langle A_{x_0} A_{\epsilon_x} A_{y_0} A_{\epsilon_y} \cos\left(\phi_{x_0} - \phi_{\epsilon_x}\right) \cos\left(\phi_{y_0} - \phi_{\epsilon_y}\right)\rangle = 2\langle x_0 y_0\rangle\langle \epsilon_x \epsilon_y\rangle + 2\langle x_0 \mathrm{H} y_0\rangle\langle \epsilon_x \mathrm{H}\epsilon_y\rangle \,. \quad (A6)$$

To establish this, we start by expanding both cosines as we did below Eq. (A4). Recognizing the signals x_0, ϵ_x and their Hilbert transform through Eqs. (A1) and (A3) allows to write

$$A_{x_0} A_{\epsilon_x} \cos\left(\phi_{x_0} - \phi_{\epsilon_x}\right) = A_{x_0} \cos\phi_{x_0} A_{\epsilon_x} \cos\phi_{\epsilon_x} + A_{x_0} \sin\phi_{x_0} A_{\epsilon_x} \sin\phi_{\epsilon_x} = x_0 \epsilon_x + \mathrm{H}x_0 \mathrm{H}\epsilon_x$$

and similarly for the y signals. Inserting these relationships into the left-hand side of Eq. (A6) yields a time average $\langle (x_0\epsilon_x + \mathrm{H}x_0\mathrm{H}\epsilon_x)\left(y_0\epsilon_y + \mathrm{H}y_0\mathrm{H}\epsilon_y\right)\rangle$. Expanding the product and using the independence of x_0, y_0 and ϵ_x, ϵ_y, we obtain

$$\langle x_0 y_0\rangle\langle \epsilon_x \epsilon_y\rangle + \langle x_0 \mathrm{H} y_0\rangle\langle \epsilon_x \mathrm{H}\epsilon_y\rangle + \langle \mathrm{H}x_0 y_0\rangle\langle \mathrm{H}\epsilon_x \epsilon_y\rangle + \langle \mathrm{H}x_0 \mathrm{H} y_0\rangle\langle \mathrm{H}\epsilon_x \mathrm{H}\epsilon_y\rangle \,.$$

It turns out that the first and last terms are equal to each other, and likewise for the second and third terms, from which Eq. (A6) follows. For example,

$$\langle x_0 y_0\rangle = \langle A_{x_0} A_{y_0} \cos\phi_{x_0} \cos\phi_{y_0}\rangle = \langle A_{x_0} A_{y_0} \frac{\cos(\phi_{x_0} + \phi_{y_0}) + \cos(\phi_{x_0} - \phi_{y_0})}{2}\rangle$$

and

$$\langle \mathrm{H}x_0 \mathrm{H} y_0\rangle = \langle A_{x_0} A_{y_0} \sin\phi_{x_0} \sin\phi_{y_0}\rangle = \langle A_{x_0} A_{y_0} \frac{-\cos(\phi_{x_0} + \phi_{y_0}) + \cos(\phi_{x_0} - \phi_{y_0})}{2}\rangle$$

both converge to the same value $\langle A_{x_0} A_{y_0} \cos\left(\delta_{x_0} - \delta_{y_0}\right)\rangle/2$ because the time average containing the high-frequency oscillation $\cos\left(\phi_{x_0} + \phi_{y_0}\right) = \cos\left(4\pi\nu_0 t + \delta_{x_0} + \delta_{y_0}\right)$ vanishes once again due to the separation of timescales.

It is noteworthy that the first term in the right-hand side of Eq. (A6) is closely related to the quantity $\mathcal{L}(x, y)$ defined in Eq. (12). More specifically,

$$\mathcal{L}(x,y) = 8\mathrm{cov}(x_0, y_0)\mathrm{cov}\big(\epsilon_x, \epsilon_y\big) = 8\langle x_0 y_0\rangle\langle \epsilon_x \epsilon_y\rangle\,. \qquad (A7)$$

The first equality follows by inserting the relationship (2) between neural and measured signals into the definition (12) and using the independence of neural and noise signals to set both $\mathrm{cov}\big(x_0, \epsilon_y\big)$ and $\mathrm{cov}(\epsilon_x, y_0)$ to zero. The second equality follows from the definition of covariance (reviewed right below Eq. 1) and the fact that all signal averages $\langle x_0\rangle$, $\langle y_0\rangle$, $\langle \epsilon_x\rangle$, and $\langle \epsilon_y\rangle$ vanish (which are particular cases of Eq. A4). Identity (A6) can then be recast as

$$\langle A_{x_0} A_{\epsilon_x} A_{y_0} A_{\epsilon_y} \cos\big(\phi_{x_0} - \phi_{\epsilon_x}\big) \cos\left(\phi_{y_0} - \phi_{\epsilon_y}\right)\rangle = \frac{\mathcal{L}(x,y) + \mathcal{L}(x,\mathrm{H}y)}{4}\,. \qquad (A8)$$

The significance of Eq. (A7) is that it establishes the claim made in the main text that $\mathcal{L}(x,y)$ is proportional to the neural zero-lag correlation R_0. Similarly, by definition (A3) of the Hilbert transform, $\mathcal{L}(x,\mathrm{H}y)$ is proportional to a measure $\mathrm{corr}[x_0, \mathrm{H}y_0]$ of neural 90-degree phase lag coupling.

A.3. Derivation of Eqs. (10) and (11)

It is slightly simpler to deal with Eq. (11) first. The idea is to insert the decomposition (8) into the defining expression of the variance of amplitude squared $\sigma^2_{A^2_x} = \mathrm{cov}(A^2_x, A^2_x)$. Expanding and gathering terms where possible, we find that $\sigma^2_{A^2_x}$ equals to

$$\sigma^2_{A^2_{x_0}} + \sigma^2_{A^2_{\epsilon_x}} + 2\mathrm{cov}\big(A^2_{x_0}, A^2_{\epsilon_x}\big) + 4\,\langle A^2_{x_0} A^2_{\epsilon_x} \cos\big(\phi_{x_0} - \phi_{\epsilon_x}\big)^2\rangle - 4\langle A_{x_0} A_{\epsilon_x} \cos\big(\phi_{x_0} - \phi_{\epsilon_x}\big)\rangle^2$$
$$+ 2\langle\big(A^2_{x_0} + A^2_{\epsilon_x}\big) A_{x_0} A_{\epsilon_x} \cos\big(\phi_{x_0} - \phi_{\epsilon_x}\big)\rangle - 2\langle A^2_{x_0} + A^2_{\epsilon_x}\rangle\langle A_{x_0} A_{\epsilon_x} \cos\big(\phi_{x_0} - \phi_{\epsilon_x}\big)\rangle\,.$$

This daunting expression simplifies, as the third term vanishes due to the independence of cerebral and noise signals and so do the fifth to last terms thanks to identities (A4). Our result (A5) takes care of the fourth term, which leads to

$$\sigma_{A_x^2}^2 = \sigma_{A_{x_0}^2}^2 + \sigma_{A_{\epsilon_x}^2}^2 + 2\langle A_{x_0}^2\rangle\langle A_{\epsilon_x}^2\rangle \,.$$

This is almost Eq. (11). To connect with it, we take the time average of the decomposition formula (8) and apply an identity (A4) to simplify the last term,

$$\langle A_x^2\rangle = \langle A_{x_0}^2\rangle + \langle A_{\epsilon_x}^2\rangle + 2\langle A_{x_0}A_{\epsilon_x}\cos\left(\phi_{x_0} - \phi_{\epsilon_x}\right)\rangle = \langle A_{x_0}^2\rangle + \langle A_{\epsilon_x}^2\rangle \,.$$

Combining the two preceding equations, we obtain

$$\sigma_{A_x^2}^2 = \sigma_{A_{x_0}^2}^2 + \sigma_{A_{\epsilon_x}^2}^2 + 2\left(\langle A_x^2\rangle - \langle A_{\epsilon_x}^2\rangle\right)\langle A_{\epsilon_x}^2\rangle$$

which is precisely Eq. (11).

The derivation of Eq. (10) follows the same line. Expanding the covariance $\mathrm{cov}\left(A_x^2, A_y^2\right)$ with the decomposition formula (8) and gathering terms leads to

$$\begin{aligned}\mathrm{cov}\left(A_{x_0}^2, A_{y_0}^2\right) + \mathrm{cov}\left(A_{x_0}^2, A_{\epsilon_y}^2\right) + \mathrm{cov}\left(A_{\epsilon_x}^2, A_{y_0}^2\right) + \mathrm{cov}\left(A_{\epsilon_x}^2, A_{\epsilon_y}^2\right)\\ + 2\mathrm{cov}\left(A_{x_0}^2 + A_{\epsilon_x}^2, A_{y_0}A_{\epsilon_y}\cos\left(\phi_{y_0} - \phi_{\epsilon_y}\right)\right) + 2\mathrm{cov}\left(A_{x_0}A_{\epsilon_x}\cos\left(\phi_{x_0} - \phi_{\epsilon_x}\right), A_{y_0}^2 + A_{\epsilon_y}^2\right)\\ + 4\mathrm{cov}\left(A_{x_0}A_{\epsilon_x}\cos\left(\phi_{x_0} - \phi_{\epsilon_x}\right), A_{y_0}A_{\epsilon_y}\cos\left(\phi_{y_0} - \phi_{\epsilon_y}\right)\right).\end{aligned}$$

Again, several simplifications take place. The second and third terms vanish due to the independence of cerebral and noise signals; the covariances in the fifth and sixth terms too since they involve averages of the form (A4). The last term also simplifies to

$$4\,\langle A_{x_0} A_{\epsilon_x} A_{y_0} A_{\epsilon_y} \cos\left(\phi_{x_0} - \phi_{\epsilon_x}\right) \cos\left(\phi_{y_0} - \phi_{\epsilon_y}\right)\rangle$$

thanks to Eq. (A4), and thus it equals to $\mathcal{L}(x, y) + \mathcal{L}(x, \mathrm{H}y)$ by our last identity (A8). Gathering these observations together, we find

$$\mathrm{cov}\left(A_x^2, A_y^2\right) = \mathrm{cov}\left(A_{x_0}^2, A_{y_0}^2\right) + \mathrm{cov}\left(A_{\epsilon_x}^2, A_{\epsilon_y}^2\right) + \mathcal{L}(x, y) + \mathcal{L}(x, \mathrm{H}y)$$

which is nothing but Eq. (10).

References

Babiloni, C., Arakaki, X., Azami, H., Bennys, K., Blinowska, K., Bonanni, L., Bujan, A., Carrillo, M.C., Cichocki, A., de Frutos-Lucas, J., Del Percio, C., Dubois, B., Edelmayer, R., Egan, G., Epelbaum, S., Escudero, J., Evans, A., Farina, F., Fargo, K., Fernández, A., Ferri, R., Frisoni, G., Hampel, H., Harrington, M.G., Jelic, V., Jeong, J., Jiang, Y., Kaminski, M., Kavcic, V., Kilborn, K., Kumar, S., Lam, A., Lim, L., Lizio, R., Lopez, D., Lopez, S., Lucey, B., Maestú, F., McGeown, W.J., McKeith, I., Moretti, D.V., Nobili, F., Noce, G., Olichney, J., Onofrj, M., Osorio, R., Parra-Rodriguez, M., Rajji, T., Ritter, P., Soricelli, A., Stocchi, F., Tarnanas, I., Taylor, J.P., Teipel, S., Tucci, F., Valdes-Sosa, M., Valdes-Sosa, P., Weiergräber, M., Yener, G., Guntekin, B., 2021. Measures of resting state EEG rhythms for clinical trials in Alzheimer's disease: Recommendations of an expert panel. Alzheimers. Dement. 17, 1528–1553. https://doi.org/doi: 10.1002/alz.12311

Baker, A.P., Brookes, M.J., Rezek, I.A., Smith, S.M., Behrens, T., Probert Smith, P.J., Woolrich, M., 2014. Fast transient networks in spontaneous human brain activity. Elife 2014, e01867. https://doi.org/10.7554/eLife.01867

Betti, V., Corbetta, M., de Pasquale, F., Wens, V., Della Penna, S., 2018. Topology of functional connectivity and hub dynamics in the beta band as temporal prior for natural vision in the human brain. J. Neurosci. 38, 3858–3871. https://doi.org/10.1523/JNEUROSCI.1089-17.2018

Biswal, B., Yetkin, F.Z., Haughton, V.M., Hyde, J.S., 1995. Functional connectivity in the motor cortex of resting human brain using echo-planar mri. Magn. Reson. Med. 34, 537–541. https://doi.org/10.1002/mrm.1910340409

Breakspear, M., Heitmann, S., Daffertshofer, A., 2010. Generative models of cortical oscillations: neurobiological implications of the Kuramoto model. Front. Hum. Neurosci. 4, 1–14. https://doi.org/10.3389/fnhum.2010.00190

Brookes, M.J., Groom, M.J., Liuzzi, L., Hill, R.M., Smith, H.J.F., Briley, P.M., Hall, E.L., Hunt, B.A.E., Gascoyne, L.E., Taylor, M.J., Liddle, P.F., Morris, P.G., Woolrich, M.W., Liddle, E.B., 2018. Altered temporal stability in dynamic neural networks underlies connectivity changes in neurodevelopment. Neuroimage 174, 563–575. https://doi.org/10.1016/j.neuroimage.2018.03.008

Brookes, M.J., O'Neill, G.C., Hall, E.L., Woolrich, M.W., Baker, A., Palazzo Corner, S., Robson, S.E., Morris, P.G., Barnes, G.R., 2014. Measuring temporal, spectral and spatial changes in electrophysiological brain network connectivity. Neuroimage 91, 282–299. https://doi.org/10.1016/j.neuroimage.2013.12.066

Brookes, M.J., Tewarie, P.K., Hunt, B.A.E., Robson, S.E., Gascoyne, L.E., Liddle, E.B., Liddle, P.F., Morris, P.G., 2016. A multi-layer network approach to MEG connectivity analysis. Neuroimage 132, 425–438. https://doi.org/10.1016/j.neuroimage.2016.02.045

Brookes, M.J., Woolrich, M., Luckhoo, H., Price, D., Hale, J.R., Stephenson, M.C., Barnes, G.R., Smith, S.M., Morris, P.G., 2011. Investigating the electrophysiological basis of resting

state networks using magnetoencephalography. Proc. Natl. Acad. Sci. U. S. A. 108, 16783–16788. https://doi.org/10.1073/pnas.1112685108

Brunel, N., 2000. Dynamics of Sparsely Connected Networks of Excitatory and Inhibitory Spiking Neurons. J. Comput. Neurosci. 8, 183–208. https://doi.org/10.1016/S0925-2312(00)00179-X

Brunel, N., Wang, X.J., 2003. What determines the frequency of fast network oscillations with irregular neural discharges? I. Synaptic dynamics and excitation-inhibition balance. J. Neurophysiol. 90, 415–430. https://doi.org/10.1152/jn.01095.2002

Cabral, J., Hugues, E., Sporns, O., Deco, G., 2011. Role of local network oscillations in resting-state functional connectivity. Neuroimage 57, 130–139. https://doi.org/10.1016/j.neuroimage.2011.04.010

Cabral, J., Kringelbach, M.L., Deco, G., 2014a. Exploring the network dynamics underlying brain activity during rest. Prog. Neurobiol. 114, 102–131. https://doi.org/10.1016/j.pneurobio.2013.12.005

Cabral, J., Kringelbach, M.L., Deco, G., 2017. Functional connectivity dynamically evolves on multiple time-scales over a static structural connectome: Models and mechanisms. Neuroimage 160, 84–96. https://doi.org/10.1016/j.neuroimage.2017.03.045

Cabral, J., Luckhoo, H., Woolrich, M., Joensson, M., Mohseni, H., Baker, A., Kringelbach, M.L., Deco, G., 2014b. Exploring mechanisms of spontaneous functional connectivity in MEG: How delayed network interactions lead to structured amplitude envelopes of band-

pass filtered oscillations. Neuroimage 90, 423–435. https://doi.org/10.1016/j.neuroimage.2013.11.047

Coquelet, N., De Tiège, X., Roshchupkina, L., Peigneux, P., Goldman, S., Woolrich, M., Wens, V., 2022. Microstates and power envelope hidden Markov modeling probe bursting brain activity at different timescales. Neuroimage 247, 118850. https://doi.org/10.1016/j.neuroimage.2021.118850

Daffertshofer, A., van Wijk, B.C.M., 2011. On the influence of amplitude on the connectivity between phases. Front. Neuroinform. 5. https://doi.org/10.3389/fninf.2011.00006

Dale, A.M., Sereno, M.I., 1993. Improved localization of cortical activity by combining EEG and MEG with MRI cortical surface reconstruction: A linear approach. J. Cogn. Neurosci. 5, 162–176. https://doi.org/10.1162/jocn.1993.5.2.162

de Pasquale, F., Della Penna, S., Sporns, O., Romani, G.L., Corbetta, M., 2016. A Dynamic Core Network and Global Efficiency in the Resting Human Brain. Cereb. Cortex 26, 4015–4033. https://doi.org/10.1093/cercor/bhv185

de Pasquale, F., Della Penna, S., Snyder, A.Z., Lewis, C., Mantini, D., Marzetti, L., Belardinelli, P., Ciancetta, L., Pizzella, V., Romani, G.L., Corbetta, M., 2010. Temporal dynamics of spontaneous MEG activity in brain networks. Proc. Natl. Acad. Sci. U. S. A. 107, 6040–6045. https://doi.org/10.1073/pnas.0913863107

de Pasquale, F., Della Penna, S., Snyder, A.Z., Marzetti, L., Pizzella, V., Romani, G.L., Corbetta, M., 2012. A Cortical Core for Dynamic Integration of Functional Networks in the

Resting Human Brain. Neuron 74, 753–764. https://doi.org/10.1016/j.neuron.2012.03.031

De Tiège, X., Op de Beeck, M., Funke, M., Legros, B., Parkkonen, L., Goldman, S., Van Bogaert, P., 2008. Recording epileptic activity with MEG in a light-weight magnetic shield. Epilepsy Res. 82, 227–231. https://doi.org/10.1016/j.eplepsyres.2008.08.011

Deco, G., Corbetta, M., 2011. The Dynamical Balance of the Brain at Rest. Neuroscientist 17, 107–123. https://doi.org/10.1177/1073858409354384

Deco, G., Jirsa, V.K., McIntosh, A.R., 2011. Emerging concepts for the dynamical organization of resting-state activity in the brain. Nat. Rev. Neurosci. 12, 43–56. https://doi.org/10.1038/nrn2961

Deco, G., Jirsa, V., McIntosh, A.R., Sporns, O., Kötter, R., 2009. Key role of coupling, delay, and noise in resting brain fluctuations. Proc. Natl. Acad. Sci. U. S. A. 106, 10302–10307. https://doi.org/10.1073/pnas.0901831106

Della Penna, S., Corbetta, M., Wens, V., de Pasquale, F., 2019. The Impact of the Geometric Correction Scheme on MEG Functional Topology at Rest. Front. Neurosci. 13. https://doi.org/10.3389/fnins.2019.01114

Engel, A.K., Gerloff, C., Hilgetag, C.C., Nolte, G., 2013. Intrinsic Coupling Modes: Multiscale Interactions in Ongoing Brain Activity. Neuron 80, 867–886. https://doi.org/10.1016/j.neuron.2013.09.038

Fischl, B., 2012. FreeSurfer. Neuroimage 62, 774–781. https://doi.org/10.1016/j.neuroimage.2012.01.021

Fox, M.D., Raichle, M.E., 2007. Spontaneous fluctuations in brain activity observed with functional magnetic resonance imaging. Nat. Rev. Neurosci. 8, 700–711. https://doi.org/10.1038/nrn2201

Fox, M.D., Snyder, A.Z., Vincent, J.L., Corbetta, M., Van Essen, D.C., Raichle, M.E., 2005. The human brain is intrinsically organized into dynamic, anticorrelated functional networks. Proc. Natl. Acad. Sci. U. S. A. 102, 9673–9678. https://doi.org/10.1073/pnas.0504136102

Fries, P., 2005. A mechanism for cognitive dynamics: Neuronal communication through neuronal coherence. Trends Cogn. Sci. 9, 474–480. https://doi.org/10.1016/j.tics.2005.08.011

Friston, K.J., Ashburner, J.T., Kiebel, S.J., Nichols, T.E., Penny, W.D., 2007. Statistical Parametric Mapping: the Analysis of Functional Brain Images. Acad. Press.

Gerstner, W., van Hemmen, J.L., Cowan, J.D., 1996. What Matters in Neuronal Locking? Neural Comput. 8, 1653–1676. https://doi.org/10.1162/neco.1996.8.8.1653

Gramfort, A., Luessi, M., Larson, E., Engemann, D.A., Strohmeier, D., Brodbeck, C., Parkkonen, L., Hämäläinen, M.S., 2014. MNE software for processing MEG and EEG data. Neuroimage 86, 446–460. https://doi.org/10.1016/j.neuroimage.2013.10.027

Halliday, D.M., Rosenberg, J.R., Amjad, A.M., Breeze, P., Conway, B.A., Farmer, S.F., 1995. A framework for the analysis of mixed time series/point process data-theory and application to the study of physiological tremor, single motor unit discharges and electromyograms. Prog. Biophys. Mol. Biol. 64, 237–278.

Hari, R., Salmelin, R., 1997. Human cortical oscillations: A neuromagnetic view through the skull. Trends Neurosci. 20, 44–49. https://doi.org/10.1016/S0166-2236(96)10065-5

Hauk, O., Stenroos, M., 2014. A framework for the design of flexible cross-talk functions for spatial filtering of EEG/MEG data: DeFleCT. Hum. Brain Mapp. 35, 1642–1653. https://doi.org/10.1002/hbm.22279

Hawellek, D.J., Schepers, I.M., Roeder, B., Engel, A.K., Siegel, M., Hipp, J.F., 2013. Altered intrinsic neuronal interactions in the visual cortex of the blind. J. Neurosci. 33, 17072–17080. https://doi.org/10.1523/JNEUROSCI.1625-13.2013

Higgins, C., Liu, Y., Vidaurre, D., Kurth-Nelson, Z., Dolan, R., Behrens, T., Woolrich, M., 2021. Replay bursts in humans coincide with activation of the default mode and parietal alpha networks. Neuron 109, 882–893. https://doi.org/10.1016/j.neuron.2020.12.007

Hipp, J.F., Hawellek, D.J., Corbetta, M., Siegel, M., Engel, A.K., 2012. Large-scale cortical correlation structure of spontaneous oscillatory activity. Nat. Neurosci. 15, 884–890. https://doi.org/10.1038/nn.3101

Hipp, J.F., Siegel, M., 2015. BOLD fMRI correlation reflects frequency-specific neuronal correlation. Curr. Biol. 25, 1368–1374. https://doi.org/10.1016/j.cub.2015.03.049

Honey, C.J., Kötter, R., Breakspear, M., Sporns, O., 2007. Network structure of cerebral cortex shapes functional connectivity on multiple time scales. Proc. Natl. Acad. Sci. U. S. A. 104, 10240–10245. https://doi.org/10.1073/pnas.0701519104

Hotelling, H., 1931. The Generalization of Student's Ratio. Ann. Math. Stat. 2, 360–378. https://doi.org/10.1214/aoms/1177732979

Hyvärinen, A., Oja, E., 2000. Independent component analysis: algorithms and applications. Neural Networks 13, 411–430. https://doi.org/10.7819/rbgn.v19i63.1905

Leong, C.W.Y., Leow, J.W.S., Grunstein, R.R., Naismith, S.L., Teh, J.Z., D'Rozario, A.L., Saini, B., 2022. A systematic scoping review of the effects of central nervous system active drugs on sleep spindles and sleep-dependent memory consolidation. Sleep Med. Rev. 62, 101605. https://doi.org/10.1016/j.smrv.2022.101605

Leopold, D.A., Murayama, Y., Logothetis, N.K., 2003. Very slow activity fluctuations in monkey visual cortex: Implications for functional brain imaging. Cereb. Cortex 13, 422–433. https://doi.org/10.1093/cercor/13.4.422

Mary, A., Bourguignon, M., Wens, V., Op de Beeck, M., Leproult, R., De Tiège, X., Peigneux, P., 2015. Aging reduces experience-induced sensorimotor plasticity. A magnetoencephalographic study. Neuroimage 104, 59–68. https://doi.org/10.1016/j.neuroimage.2014.10.010

Mary, A., Wens, V., Op De Beeck, M., Leproult, R., De Tiège, X., Peigneux, P., 2017. Resting-state Functional Connectivity is an Age-dependent Predictor of Motor Learning Abilities. Cereb. Cortex 27, 4923–4932. https://doi.org/10.1093/cercor/bhw286

Muthukumaraswamy, S.D., Singh, K.D., 2011. A cautionary note on the interpretation of phase-locking estimates with concurrent changes in power. Clin. Neurophysiol. 122, 2324–2325. https://doi.org/10.1016/j.clinph.2011.04.003

Naeije, G., Wens, V., Coquelet, N., Sjøgård, M., Goldman, S., Pandolfo, M., De Tiège, X.P., 2019. Age of onset determines intrinsic functional brain architecture in Friedreich ataxia. Ann. Clin. Transl. Neurol. 7, 94–104. https://doi.org/10.1002/acn3.50966

O'Neill, G.C., Barratt, E.L., Hunt, B.A.E., Tewarie, P.K., Brookes, M.J., 2015a. Measuring electrophysiological connectivity by power envelope correlation: A technical review on MEG methods. Phys. Med. Biol. 60, R271–R295. https://doi.org/10.1088/0031-9155/60/21/R271

O'Neill, G.C., Bauer, M., Woolrich, M.W., Morris, P.G., Barnes, G.R., Brookes, M.J., 2015b. Dynamic recruitment of resting state sub-networks. Neuroimage 115, 85–95. https://doi.org/10.1016/j.neuroimage.2015.04.030

O'Neill, G.C., Tewarie, P.K., Colclough, G.L., Gascoyne, L.E., Hunt, B.A.E., Morris, P.G., Woolrich, M.W., Brookes, M.J., 2017. Measurement of dynamic task related functional networks using MEG. Neuroimage 146, 667–678. https://doi.org/10.1016/j.neuroimage.2016.08.061

Oldfield, R.C., 1971. The assessment and analysis of handedness: The Edinburgh inventory. Neuropsychologia 9, 97–113. https://doi.org/10.1016/0028-3932(71)90067-4

Pfurtscheller, G., Lopes da Silva, F.H., 1999. Event-related EEG/MEG synchronization and desynchronization: Basic principles. Clin. Neurophysiol. 110, 1842–1857. https://doi.org/10.1016/S1388-2457(99)00141-8

Puttaert, D., Coquelet, N., Wens, V., Peigneux, P., Fery, P., Rovai, A., Trotta, N., Sadeghi, N., Coolen, T., Bier, J.C., Goldman, S., De Tiège, X., 2020. Alterations in resting-state network dynamics along the Alzheimer's disease continuum. Sci. Rep. 10, 21990. https://doi.org/10.1038/s41598-020-76201-3

Quinn, A.J., Vidaurre, D., Abeysuriya, R., Becker, R., Nobre, A.C., Woolrich, M.W., 2018. Task-evoked dynamic network analysis through Hidden Markov Modeling. Front. Neurosci. 12, 1–17. https://doi.org/10.3389/fnins.2018.00603

Roshchupkina, L., Wens, V., Coquelet, N., de Tiege, X., Peigneux, P., 2022. Resting state fast brain dynamics predict interindividual variability in motor performance. Sci. Rep. 12, 5340. https://doi.org/10.1038/s41598-022-08767-z

Sadaghiani, S., Brookes, M.J., Baillet, S., 2022. Connectomics of human electrophysiology. Neuroimage 247, 118788. https://doi.org/10.1016/j.neuroimage.2021.118788

Seedat, Z.A., Quinn, A.J., Vidaurre, D., Liuzzi, L., Gascoyne, L.E., Hunt, B.A.E., O'Neill, G.C., Pakenham, D.O., Mullinger, K.J., Morris, P.G., Woolrich, M.W., Brookes, M.J., 2020. The role of transient spectral 'bursts' in functional connectivity: A

magnetoencephalography study. Neuroimage 209, 116537. https://doi.org/10.1016/j.neuroimage.2020.116537

Siegel, M., Donner, T.H., Engel, A.K., 2012. Spectral fingerprints of large-scale neuronal interactions. Nat. Rev. Neurosci. 13, 121–134. https://doi.org/10.1038/nrn3137

Sitnikova, T.A., Hughes, J.W., Ahlfors, S.P., Woolrich, M.W., Salat, D.H., 2018. Short timescale abnormalities in the states of spontaneous synchrony in the functional neural networks in Alzheimer's disease. NeuroImage Clin. 20, 128–152. https://doi.org/10.1016/j.nicl.2018.05.028

Sjøgård, M., De Tiège, X., Mary, A., Peigneux, P., Goldman, S., Nagels, G., van Schependom, J., Quinn, A.J., Woolrich, M.W., Wens, V., 2019. Do the posterior midline cortices belong to the electrophysiological default-mode network? Neuroimage 200, 221–230. https://doi.org/10.1016/j.neuroimage.2019.06.052

Sjøgård, M., Wens, V., Van Schependom, J., Costers, L., D'hooghe, M., D'haeseleer, M., Woolrich, M., Goldman, S., Nagels, G., De Tiège, X., 2020. Brain dysconnectivity relates to disability and cognitive impairment in multiple sclerosis. Hum. Brain Mapp. 42, 626–643. https://doi.org/10.1002/hbm.25247

Smith, S.M., Fox, P.T., Miller, K.L., Glahn, D.C., Fox, P.M., Mackay, C.E., Filippini, N., Watkins, K.E., Toro, R., Laird, A.R., Beckmann, C.F., 2009. Correspondence of the brain's functional architecture during activation and rest. Proc. Natl. Acad. Sci. U. S. A. 106, 13040–13045. https://doi.org/10.1073/pnas.0905267106

Taulu, S., Simola, J., Kajola, M., 2005. Application of the signal space separation method. IEEE Trans. Signal Process 53, 3359–3372.

Tewarie, P., Bright, M.G., Hillebrand, A., Robson, S.E., Gascoyne, L.E., Morris, P.G., Meier, J., Van Mieghem, P., Brookes, M.J., 2016. Predicting haemodynamic networks using electrophysiology: The role of non-linear and cross-frequency interactions. Neuroimage 130, 273–292. https://doi.org/10.1016/j.neuroimage.2016.01.053

Tewarie, P., Abeysuriya, R., Byrne, Á., O'Neill, G.C., Sotiropoulos, S.N., Brookes, M.J., Coombes, S., 2019. How do spatially distinct frequency specific MEG networks emerge from one underlying structural connectome? The role of the structural eigenmodes. Neuroimage 186, 211–220. https://doi.org/10.1016/j.neuroimage.2018.10.079

Tewarie, P., Hunt, B.A.E., O'Neill, G.C., Byrne, A., Aquino, K., Bauer, M., Mullinger, K.J., Coombes, S., Brookes, M.J., 2018. Relationships between Neuronal Oscillatory Amplitude and Dynamic Functional Connectivity. Cereb. Cortex 29, 2668–2681. https://doi.org/10.1093/cercor/bhy136

Van Dyck, D., Deconinck, N., Aeby, A., Baijot, S., Coquelet, N., Trotta, N., Rovai, A., Goldman, S., Urbain, C., Wens, V., De Tiège, X., 2021a. Atypical resting-state functional brain connectivity in children with developmental coordination disorder. NeuroImage Clin. 33, 102928. https://doi.org/10.1016/j.nicl.2021.102928

Van Dyck, D., Deconinck, N., Aeby, A., Baijot, S., Coquelet, N., Trotta, N., Rovai, A., Goldman, S., Urbain, C., Wens, V., De Tiège, X., 2021b. Resting-state functional brain connectivity is

related to subsequent procedural learning skills in school-aged children. Neuroimage 240, 118368. https://doi.org/10.1016/j.neuroimage.2021.118368

van Ede, F., Quinn, A.J., Woolrich, M.W., Nobre, A.C., 2018. Neural Oscillations: Sustained Rhythms or Transient Burst-Events? Trends Neurosci. 41, 415–417. https://doi.org/10.1016/j.tins.2018.04.004

Van Schependom, J., Vidaurre, D., Costers, L., Sjøgård, M., D'hooghe, M.B., D'haeseleer, M., Wens, V., De Tiège, X., Goldman, S., Woolrich, M., Nagels, G., 2019. Altered transient brain dynamics in multiple sclerosis: Treatment or pathology? Hum. Brain Mapp. 40, 4789–4800. https://doi.org/10.1002/hbm.24737

van Vreeswijk, C., Sompolinsky, H., 1996. Chaos in neuronal networks with balanced excitatory and inhibitory activity. Science (80-.). 274, 1724–1726. https://doi.org/10.1126/science.274.5293.1724

Vander Ghinst, M., Bourguignon, M., Op de Beeck, M., Wens, V., Marty, B., Hassid, S., Choufani, G., Jousmäki, V., Hari, R., Van Bogaert, P., Goldman, S., De Tiège, X., 2016. Left superior temporal gyrus is coupled to attended speech in a cocktail-party auditory scene. J. Neurosci. 36, 1596–1606. https://doi.org/10.1523/JNEUROSCI.1730-15.2016

Vidaurre, D., Hunt, L.T., Quinn, A.J., Hunt, B.A.E., Brookes, M.J., Nobre, A.C., Woolrich, M.W., 2018. Spontaneous cortical activity transiently organises into frequency specific phase-coupling networks. Nat. Commun. 9, 2987. https://doi.org/10.1038/s41467-018-05316-z

Vigario, R., Sarela, J., Jousmäki, V., Hämäläinen, M., Oja, E., 2000. Independent component approach to the analysis of EEG and MEG recordings. IEEE Trans. Biomed. Eng. 47, 589–593.

Wens, V., Mary, A., Bourguignon, M., Goldman, S., Marty, B., Op de Beeck, M., Van Bogaert, P., Peigneux, P., De Tiège, X., 2014a. About the electrophysiological basis of resting state networks. Clin. Neurophysiol. 125, 1711–1713. https://doi.org/10.1016/j.clinph.2013.11.039

Wens, V., 2015. Investigating complex networks with inverse models: Analytical aspects of spatial leakage and connectivity estimation. Phys. Rev. 91, 012823.

Wens, V., Bourguignon, M., Goldman, S., Marty, B., Op De Beeck, M., Clumeck, C., Mary, A., Peigneux, P., Van Bogaert, P., Brookes, M.J., De Tiège, X., 2014b. Inter- and Intra-Subject Variability of Neuromagnetic Resting State Networks. Brain Topogr. 27, 620–634. https://doi.org/10.1007/s10548-014-0364-8

Wens, V., Bourguignon, M., Vander Ghinst, M., Mary, A., Marty, B., Coquelet, N., Naeije, G., Peigneux, P., Goldman, S., De Tiège, X., 2019. Synchrony, metastability, dynamic integration, and competition in the spontaneous functional connectivity of the human brain. Neuroimage 199, 313–324. https://doi.org/10.1016/j.neuroimage.2019.05.081

Wens, V., Marty, B., Mary, A., Bourguignon, M., Op de Beeck, M., Goldman, S., Van Bogaert, P., Peigneux, P., De Tiège, X., 2015. A geometric correction scheme for spatial leakage effects in MEG/EEG seed-based functional connectivity mapping. Hum. Brain Mapp. 36, 4604–4621.

Wilson, H.R., Cowan, J.D., 1972. Excitatory and Inhibitory Interactions in Localized Populations of Model Neurons. Biophys. J. 12, 1–24.